

Superresolution microscopy reveals photoreceptor-specific subciliary location and function of ciliopathy-associated protein, Cep290

Valencia L. Potter, ... , Michael A. Robichaux, Theodore G. Wensel

JCI Insight. 2021. <https://doi.org/10.1172/jci.insight.145256>.

Research In-Press Preview Cell biology Ophthalmology

Mutations in the cilium-associated protein CEP290 cause retinal degeneration as part of multi-organ ciliopathies or as retina-specific diseases. The precise location and the functional roles of CEP290 within cilia and, specifically, the connecting cilia (CC) of photoreceptors, remain unclear. We used superresolution fluorescence microscopy and electron microscopy (TEM) to localize CEP290 in the CC and in primary cilia of cultured cells with sub-diffraction resolution, and to determine effects of CEP290 deficiency in three mutant models. Radially, CEP290 localizes in close proximity to the microtubule doublets in the region between the doublets and the ciliary membrane. Longitudinally, it is distributed throughout the length of the CC whereas it is confined to the very base of primary cilia in hRPE-1 cells. We found Y-shaped links, ciliary sub-structures between microtubules and membrane, throughout the length of the CC. Severe CEP290 deficiencies in mouse models did not prevent assembly of cilia or cause obvious mislocalization of ciliary components in early stages of degeneration. There were fewer cilia and no normal outer segments in the mutants, but the Y-shaped links were clearly present. These results point to photoreceptor-specific functions of CEP290 essential for CC maturation and stability following the earliest stages of ciliogenesis.

Find the latest version:

<https://jci.me/145256/pdf>



1 **Superresolution microscopy reveals photoreceptor-specific subciliary location**
2 **and function of ciliopathy-associated protein, Cep290**

3
4 Valencia L. Potter^{1,2,3,4,5}, Abigail R. Moye^{1,4}, Michael A. Robichaux^{1,6}, Theodore G.
5 Wensel¹

6
7 ¹Verna and Marrs McLean Department of Biochemistry and Molecular Biology, Baylor
8 College of Medicine, 1 Baylor Plaza, Houston, TX, 77030

9 ²Program in Developmental Biology, Baylor College of Medicine, 1 Baylor Plaza,
10 Houston, TX, 77030

11 ³Medical Scientist Training Program (MSTP), Baylor College of Medicine, 1 Baylor
12 Plaza, Houston, TX, 77030

13 ⁴Equal Contributions

14 ⁵Current Address: Department of Ophthalmology, University Hospitals Cleveland
15 Medical Center, 11100 Euclid Avenue, Cleveland, OH, 44106

16 ⁶Departments of Ophthalmology and Biochemistry, West Virginia University, 108
17 Biomedical Road, Morgantown, WV, 26506

18 Keywords: Connecting Cilium, CEP290, SIM, STORM, *Cep290*^{rd16}, Y-shaped links

19
20 Corresponding Author: Theodore G Wensel, One Baylor Plaza, BCM125, Houston, TX
21 77030; voice:713-798-6994; email: twensel@bcm.edu

22 The authors have declared that no conflicts of interest exist.

23

168

169 **Abstract**

170 Mutations in the cilium-associated protein CEP290 cause retinal degeneration as part of
171 multi-organ ciliopathies or as retina-specific diseases. The precise location and the
172 functional roles of CEP290 within cilia and, specifically, the connecting cilia (CC) of
173 photoreceptors, remain unclear. We used superresolution fluorescence microscopy and
174 electron microscopy (TEM) to localize CEP290 in the CC and in primary cilia of cultured
175 cells with sub-diffraction resolution, and to determine effects of CEP290 deficiency in
176 three mutant models. Radially, CEP290 localizes in close proximity to the microtubule
177 doublets in the region between the doublets and the ciliary membrane. Longitudinally, it
178 is distributed throughout the length of the CC whereas it is confined to the very base of
179 primary cilia in hRPE-1 cells. We found Y-shaped links, ciliary sub-structures between
180 microtubules and membrane, throughout the length of the CC. Severe CEP290
181 deficiencies in mouse models did not prevent assembly of cilia or cause obvious
182 mislocalization of ciliary components in early stages of degeneration. There were fewer
183 cilia and no normal outer segments in the mutants, but the Y-shaped links were clearly
184 present. These results point to photoreceptor-specific functions of CEP290 essential for
185 CC maturation and stability following the earliest stages of ciliogenesis.

186

187 **Introduction**

188 Ciliopathies, genetic defects in components of primary and motile cilia, lead to a host of
189 diseases with diverse presentations, which reflect the diverse functions of cilia (1, 2).
190 Primary cilia, non-motile, hair-like protrusions found on virtually all mammalian cells, are
191 elaborate structures with hundreds of protein constituents that function as cell antennae,
192 collecting and relaying external stimuli to regulate cellular processes and maintain
193 homeostasis. An interesting subset of ciliopathy genes can be associated either with
194 multi-syndromic disease, often including retinal degeneration, or with retina-specific
195 disease (3), depending on the allele, and possibly on the genetic background and other
196 factors. Little is known about the factors that determine the precise manifestations of
197 each ciliopathy, or about the pathophysiological mechanisms involved in retinal
198 degeneration. The occurrence of different ciliopathy phenotypes likely depends on the
199 precise positioning of structural and functional components.

200 Defects in the gene encoding centrosomal protein of 290 kDa (*CEP290*) are the
201 leading genetic cause of the severe blinding condition known as Leber Congenital
202 Amaurosis (LCA) (4-7). In addition to LCA, different *CEP290* mutations can give rise to
203 non-syndromic retinitis pigmentosa (8) and multisyndromic disorders with associated
204 retinal degeneration, such as Bardet-Biedl syndrome and Meckel-Gruber syndrome (5,
205 9-14). Understanding the functions of the protein CEP290, both in photoreceptor
206 sensory cilia and in other primary cilia, is critical to understanding these diseases, and
207 to guiding therapeutic interventions and genetic counseling.

208 Primary cilia nucleate from a mother centriole at the apical surface of the cell and have
209 a specialized region at their base called the transition zone, beyond which extends the

210 ciliary axoneme, a bundle of 9 + 0 microtubule doublets. The transition zone ranges
211 from ~200-300 nm in length and is ~300 nm in diameter, depending on cell type (1, 2,
212 15-18). Within the transition zone, there are filamentous structures extending from the
213 outer surface of the axonemal microtubules to the ciliary membrane, often referred to as
214 Y-shaped links or Y-links (the term used throughout here) because of their appearance
215 in electron micrographs of ciliary cross-sections stained with heavy metals (19, 20).
216 Recent electron tomographic studies suggest that their true structures in three
217 dimensions are not very “Y-like” but confirm that they are narrower at the microtubule-
218 end with wider bifurcations at the membrane (21, 22). The molecular composition of
219 these structures is unknown. The ciliary membrane, while continuous with the plasma
220 membrane, contains a unique set of membrane proteins such as ion channels and
221 receptors (15, 23, 24). An elaborate but poorly understood network of molecular
222 machinery within the primary cilium is necessary to ensure proper transport and
223 distribution of ciliary components and to prevent mis-accumulation of non-ciliary
224 proteins.

225 Among the numerous cell types that rely on primary cilia for proper functioning,
226 rod and cone photoreceptor cells of the vertebrate retina carry out their entire
227 phototransduction cascade within their cilia, making cilia essential for vision (reviewed in
228 (25)). The modified primary cilia of photoreceptors contain a light-sensing outer
229 segment and the connecting cilium (CC), which connects the outer and inner segments.
230 The axoneme extends from the CC into the outer segment, with microtubules extending
231 first as doublets, and then as singlets. The light-sensing disc membranes are anchored
232 to the axonemal microtubules. Since proteins are synthesized in the inner segment of

233 photoreceptor cells, the CC is an essential region for the trafficking of phototransduction
234 proteins to the outer segment. The mouse CC is ~1100 nm in length and ~300 nm in
235 diameter (Figure 1) (26). Inside the ring of nine microtubule doublets is the lumen,
236 containing calcium-binding proteins called centrins (27-31), and extending from the
237 doublets to the ciliary membrane are the Y- links (Figure 1D), which have been
238 proposed to aid in maintaining the structural integrity of the CC (32). The distribution of
239 Y-links along the length of the CC has not been unequivocally determined; in most
240 ciliated cells they are restricted to the basal region of the cilia as densities that connect
241 the axoneme and membrane, often lacking strict 9-fold symmetry. However,
242 connections have been observed throughout the length of some primary cilia (21). The
243 structures of the Y-links in the CC and other mammalian primary cilia appear similar, but
244 in no cell-type are their molecular components known.

245 CEP290 has been localized to rod CC, and based on studies *in vitro* and in
246 motile cilia (e.g., *Chlamydomonas* flagella, where it is also known as POC3), it has been
247 proposed to play important roles in ciliogenesis, protein recruitment to the centriolar
248 satellites, structural support of the cilium, and regulation of ciliary protein trafficking (33-
249 35). The function of CEP290 in photoreceptors, however, remains uncertain. It has
250 recently been proposed that retina-specific ciliopathies can arise from defects in retina-
251 specific structures or aberrations in spatial distributions of components within the
252 sensory cilia (outer segments plus CC) of rods and cones. In a recent study using
253 methods similar to those employed here, we observed that a number of ciliary
254 components, including CEP290, undergo photoreceptor-specific re-distribution in the
255 absence of the product of another LCA-associated gene, *Spata7* (36). These results

256 and the spectrum of CEP290-associated disease suggest there may be functions of
257 CEP290 that are specific to retinal photoreceptor cilia.

258 A limitation of most previous studies examining localization of CEP290 in
259 photoreceptors has been the resolution limit of conventional light microscopy. Given that
260 the entire width of the CC is approximately 300 nm, only slightly wider than the ~250 nm
261 full width at half maximum (FWHM) of the narrowest point-spread function practically
262 achievable in a confocal microscope (37), imaging methods beyond the diffraction limit
263 are needed to determine sub-ciliary distributions of CEP290 and its binding partners in
264 wild type and *Cep290* mutant animals. Given the narrow dimensions of the cilium, we
265 used superresolution light microscopy – structured illumination microscopy (SIM) and
266 stochastic optical reconstruction microscopy (STORM) (38, 39) – to localize CEP290
267 precisely within the sub-compartments of wild type and *Cep290* mutant rod CC, as well
268 as in primary cilia of cultured epithelial cells. We used the same techniques to examine
269 the effects of CEP290 deficiencies on the localization of ciliary components in mouse
270 ciliopathy models. Finally, we correlated our fluorescence localization results with new
271 electron microscopic data revealing ciliary structures at even higher resolution.

272

273

274 **Results**

275 *CEP290 localizes throughout the length of the connecting cilium and in close proximity*
276 *to the microtubule doublets.* To determine the spatial distribution of CEP290 within the
277 CC, mouse retinas and retinal sections from adult animals (six weeks to eight months)
278 were co-labeled with antibodies for CEP290 and cilia markers with known distributions.
279 To distinguish CC staining from inner segment staining, we used CEP164, a protein
280 whose antibodies label the transition fibers/distal appendages, structures located at the
281 inner segment (IS)/CC interface (40). We used an antibody specific for centrins, a set of
282 calcium-binding proteins known to be centrally localized throughout the length of the CC
283 (27-31, 41), to calibrate the length of the axoneme (Figure 2A). To quantify the extent of
284 CEP290 localization along the length of the CC and to compare it to that of centrin
285 localization, we measured the distances between the proximal and distal boundaries of
286 CEP290 signal (Figure 2B), defined as the positions near the edges where signal was
287 33% of its maximal value for SIM and STORM, respectively. When measured from the
288 IS/CC interface, marked by CEP164, the average lengths of centrin and CEP290
289 labeling were similar in SIM: 984 nm \pm 201 nm and 1033 nm \pm 200 nm, respectively. In
290 STORM, the average lengths were 1193 nm \pm 168 nm and 1336 nm \pm 248 nm,
291 respectively (Figure 2G), suggesting that CEP290's localization may extend to the base
292 of the outer segment, beyond the distal boundary of centrin. The small differences in
293 length between the two imaging modalities can be explained by the differential
294 stretching or shrinking of structures in the very different fixation and imaging media used
295 for each method. These values are in agreement with previously reported
296 measurements of CC length (26), and indicate that CEP290 localizes throughout the

297 length of the CC. This finding is in contrast with its localization in other primary cilia, as
298 discussed below, and indicates that the functional role of CEP290 in photoreceptors is
299 performed throughout the entire CC and is not restricted to the base of the transition
300 zone, as it is in the transition zones of other characterized cilia.

301 To determine the radial distribution of CEP290, we co-labeled retinas with
302 antibodies for centrins, which localize to the central-most compartment of the
303 connecting cilium, acetylated α -tubulin (AcTub), which labels the microtubule doublets
304 of the axoneme (42), and wheat germ agglutinin (WGA), a lectin which binds to the
305 glycoproteins of the ciliary membrane (43). Cross sections through the CC imaged with
306 SIM revealed that CEP290 localized outside the region of the lumen (Figure 2C).
307 Longitudinal SIM images (Figure 2D-F) depict the width of the CEP290 signal as greater
308 than the centrin and AcTub signal widths, while STORM images depict the widths of the
309 CEP290 and AcTub signals as the same but wider than the centrin signal and within the
310 WGA-stained membrane of the CC. Radial measurements of the labeled areas in
311 longitudinal images, measured from the center of the cilium to the position of 33% of
312 maximal signal for SIM and STORM, are shown in Figure 2H. The average maximal
313 radii of centrin and AcTub were $87 \text{ nm} \pm 14 \text{ nm}$ and $91 \text{ nm} \pm 14 \text{ nm}$, respectively, from
314 SIM images, and were $66 \text{ nm} \pm 9 \text{ nm}$ and $109 \text{ nm} \pm 17 \text{ nm}$, respectively, from STORM
315 reconstructions. These values are in agreement with previously reported radial
316 measurements of the CC (26). The radius of CEP290 staining measured $137 \text{ nm} \pm 28$
317 nm and $107 \text{ nm} \pm 25 \text{ nm}$ in SIM and STORM, respectively. The small difference may
318 reflect differences in sample preparation as suggested above, possibly leading to
319 differential staining of CEP290 in different sub-regions of the CC in each method.

320 Interestingly, the distribution of CEP290 signal was, in many cases, not symmetric
321 about the central axis of the CC as would be expected for a protein in solution with a
322 uniform concentration, but rather, was shifted either to the left or the right of the central
323 axis (Supplemental Figure 1). Both the width of CEP290 we observe by STORM and
324 the asymmetry of its staining pattern are consistent with recently reported STORM
325 images collected from cross-sectional views of centrioles in RPE-1 cells (44), but
326 narrower than the ~250 nm width observed by STED microscopy of longitudinal views in
327 the same cell type (18), which is more consistent with our SIM results. Figure 21
328 summarizes schematically the longitudinal and radial distribution of CEP290 within the
329 rod CC. These results indicate that CEP290 localizes in close proximity to the
330 microtubule doublets, likely in a regular structural pattern throughout the CC.

331 *Y-links localize throughout the length of the connecting cilium.* Y-links are ill-defined
332 fibrous structures that radiate from each microtubule doublet pair to the ciliary
333 membrane. CEP290 has been proposed to provide structural stability to the transition
334 zone in primary cilia by contributing to or forming the Y-links (45). To investigate
335 whether the Y-links of the photoreceptor CC localize to the same subcellular
336 compartment as CEP290, *i.e.* throughout the length of the CC and in the region
337 between the microtubules and the membrane, we performed transmission electron
338 microscopy on sections cut as nearly perpendicular as possible to the ciliary axes. We
339 imaged multiple cross-sectional CCs near to or overlapping with the base of the outer
340 segment (Figure 3A). As expected, our images show Y-links in the proximal CC,
341 identified by the absence of discs and outer segment membrane (Figure 3B-C). We also
342 found that Y-links are present in the distal CC, a plane identified by the presence of

343 outer segment discs *en face*, indicating that the sections were not cut obliquely. Present
344 within the same plane were examples in which the fusion of the CC membrane with the
345 outer segment membrane can be seen (Figure 3D). Thus, our data show that Y-links
346 are present throughout the length of the CC, consistent with the longitudinal distribution
347 of CEP290. These findings are also in agreement with previously reported studies using
348 electron microscopic techniques on photoreceptors (46-48), although those did not
349 clearly demonstrate Y-links in the distal CC at the base of OS.

350 *CEP290 localizes to the base of the ciliary transition zone in non-photoreceptor primary*
351 *cilia.* To compare CEP290 localization in the CC to that in primary cilia of non-
352 photoreceptor cells, we examined CEP290 localization in primary cilia of epithelial cells.
353 Human retinal pigment epithelium (hRPE-1) cells are cultured cells that form primary
354 cilia upon serum starvation. Previously, it was reported that CEP290 did not precisely
355 localize with other transition zone proteins in hRPE-1 cells, and that, instead, CEP290
356 localized between the basal body and the other transition zone proteins (18). We used
357 SIM to image ciliated hRPE-1 cells immunolabeled with centrin antibody to identify the
358 basal body (centrin in hRPE-1 cells is restricted to the basal body, and not the lumen of
359 the ciliary axoneme as in rod CC), with acetylated α -tubulin (AcTub) antibody to label
360 the axoneme, with MKS3 (18, 49, 50), and NPHP8 (18, 51, 52) components of the MKS
361 and NPHP modules, respectively, to identify the distal transition zone, and with CEP164
362 antibodies to mark the transition fibers/distal appendages, radial structures attached to
363 the distal end of the mother centriole in the BB (44). Consistent with previous reports
364 (18, 33, 44), CEP290 and CEP164 localize below the base of the cilium in hRPE-1 cells
365 (Figure 4A-B). In both cases, CEP290 and CEP164 labeling appeared more proximal

366 than AcTub labeling (Figure 4A-B; Supplemental Figure 4). NPHP8 and MKS3 localize
367 to the cilium and distal basal body (Figure 4C-D). On average, the distance between the
368 distal edge of CEP290 and the distal edge of centrin was $64 \text{ nm} \pm 54 \text{ nm}$ ($n=20$) (Figure
369 4E), while the distance between the proximal edge of CEP290 and the proximal edge of
370 AcTub, was $-84 \text{ nm} \pm 129 \text{ nm}$ ($n = 72$) (Figure 4F). Thus, the CEP290 signal in hRPE-1
371 cilia partially overlaps with centrin and AcTub at the base of the cilium. The average
372 extent of CEP164 beyond centrin was $-24 \text{ nm} \pm 71 \text{ nm}$ ($n=10$) (Figure 4E); *i.e.*, the distal
373 edge of CEP164 staining is on average more proximal than the distal edge of centrin
374 staining. The distance between the proximal borders of CEP164 and AcTub was -106
375 $\text{nm} \pm 81 \text{ nm}$ ($n = 28$) (Figure 4F). CEP164 signal in hRPE-1 cells primarily overlaps with
376 centrin. MKS3 and NPHP8 were $10\text{nm} \pm 78\text{nm}$ ($n=42$) and $-8\text{nm} \pm 101\text{nm}$ ($n=42$)
377 proximal to AcTub labeling, respectively, and $145\text{nm} \pm 70\text{nm}$ ($n=32$) and $133\text{nm} \pm 78\text{nm}$
378 ($n=32$) beyond centrin labeling, respectively. The proximal borders of MKS3 and NPHP8
379 signal in hRPE-1 primarily overlap with that of AcTub. Figure 4G illustrates
380 schematically CEP290 localization in hRPE-1 primary cilia in relation to centrin,
381 CEP164, MKS3, NPHP8 and AcTub. These results suggest that CEP290 in the primary
382 cilia of epithelial cells is predominantly located at the base of the axoneme, overlapping
383 with but partially distal to CEP164 and centrin, and does not extend throughout the
384 entire transition zone, as demarcated by MKS3 and NPHP8, consistent with previous
385 results obtained by superresolution fluorescence (18). These results are strikingly
386 different from those obtained in rod cells (Figure 5), supporting the idea of
387 photoreceptor-specific functions for CEP290 in the CC.

388 These results are also consistent with the hypothesis that CEP290 is associated with
389 the Y-links, because, as shown in a recent electron tomographic study of primary cilia in
390 a different epithelial cell line (IMCD3 cells), structures corresponding to Y-links were
391 observed only within the first one hundred nanometers of the transition zone (21),
392 although various structures connecting the axoneme and membrane were found beyond
393 that point. To further test this idea that CEP290 has distinct localization within the rod
394 CC as compared to its distribution in other primary cilia, we compared the localization of
395 NPHP8, CEP290 and acetylated α -tubulin in primary cilia of hRPE-1 cells and CC
396 (Figure 5 and Supplemental Figure 2) using SIM. In both cell types, CEP290 is distal to
397 the transition fibers (Figures. 2A, 2B, 4B); however, in epithelial cell cilia, CEP290 signal
398 is ~200nm in length, whereas in the CC, CEP290 is ~1100nm in length, the full length of
399 the CC. NPHP8 was seen to localize to the proximal end of the cilium in both primary
400 cilia and CC. In primary cilia, NPHP8 localization is distal to CEP290, whereas in the
401 CC, NPHP8 is not distal to CEP290 and did not display localization throughout the
402 entire CC (Figure 5). These results point to the possibility that CEP290, and other
403 transition zone markers that have been found to localize throughout the length of the
404 CC such as RPGR, (53), RPGRIP1, SPATA7, NPHP1 and NPHP4 (36), have a
405 photoreceptor-specific function, and that the CC is not simply an expanded transition
406 zone.

407 *The connecting cilium develops in CEP290 mutants prior to retinal degeneration.* We
408 next asked how mutations in *Cep290* affect CEP290 protein localization and CC
409 morphology in rod neurons. Leber Congenital Amaurosis (LCA) is a non-syndromic
410 retinal disease that results in blindness or severe visual impairment in humans within

411 the first year of life. One intronic *Cep290* mutation that leads to insertion of a cryptic
412 stop codon and protein truncation at position 998, accounts for roughly 20% of LCA
413 cases (6). *Cep290*^{rd16/rd16} (hereafter referred to as *Rd16*) mice also display signs of a
414 non-syndromic retinal disease and, thus, are commonly used as a model for LCA (54,
415 55). The *Rd16* allele contains an in-frame 300 amino acid deletion that overlaps with the
416 putative microtubule binding domain of CEP290 (56). *Rd16* mice undergo rapid
417 photoreceptor degeneration and develop abnormal, rudimentary outer segments prior to
418 degeneration. There are two other CEP290 mutant mice we evaluated in this
419 manuscript: a *Cep290*^{tm1.1Jgg} mutant and a knockout (KO) of CEP290. The
420 *Cep290*^{tm1.1Jgg/tm1.1Jgg} mouse is a model for Joubert syndrome (57) with rapid
421 photoreceptor degeneration and vermal hypoplasia (57). Joubert syndrome is a
422 syndromic ciliopathy characterized by nephronophthisis, cerebellar vermis aplasia, and
423 retinal degeneration (58). These *Cep290*^{tm1.1Jgg/tm1.1Jgg} animals will be referred to
424 throughout the rest of the paper as a near-null (NN), because an alternatively spliced
425 variant of the mutant allele may result in low residual levels of a truncated CEP290 (59).
426 The *Cep290* knockout (*Cep290*^{tm1Asw/tm1Asw}, hereinafter referred to as KO) mouse is also
427 a model for Joubert syndrome and was generated by inserting a β -gal-neo cassette in
428 place of exons 1-4 in the *Cep290* allele. The KO mice have hydrocephalus, rapid retinal
429 degeneration, mild renal disease, and premature death (60).

430 To determine whether mutations in or loss of *Cep290* affects localization of
431 CEP290 or other CC proteins, we assessed age-matched mutants and wild type (WT)
432 animals using superresolution microscopy. Since photoreceptor discs begin to form at
433 postnatal day ~7 (P7) and the *Rd16* mutant animals undergo photoreceptor cell death

434 as early as P14 (55, 60) (Supplemental Figure 3), we used P10 animals to assess CC
435 protein localization prior to photoreceptor degeneration; we found that this age provided
436 the best balance between formation of cilia and cell death (Supplemental Figure 3).

437 Surprisingly, at this early age, the CC markers we tested were only mildly
438 mislocalized in the *Rd16*, NN, and KO mutant rods compared to WT. Centrin was
439 localized throughout the CC lumen in WT and mutant cilia (Figure 6B, D, F, H), although
440 the length of centrin staining was generally shorter in mutant CCs. AcTub labeling of
441 microtubule doublets in the CC and axoneme in WT rod cilia (Figure 1B-C, Figure 6A),
442 was similar in the CC and the rudimentary outer segments of the mutant retinas (Figure
443 6C, E, G).

444 Using a C-terminal CEP290 antibody, CEP290 protein was localized
445 longitudinally throughout the CC and radially between the axoneme and the ciliary
446 membrane of WT and mutant *Rd16* rods (Figure 6A-D), indicating that the missing
447 CEP290 domain is not essential for CEP290 localization. We observed little or no
448 labeling with the C-terminal CEP290 antibody in NN or KO retinas at P10 (Figure 6E-
449 H); this finding was confirmed with western blotting (Figure 6K).

450 To quantify the difference in distributions of centrin, AcTub, and CEP290, we
451 measured the length and radius of antibody labeling in mutant and age-matched WT
452 controls. Although P10 animals have developed CC, ciliogenesis is not yet complete at
453 this age, and the ciliary dimensions are not necessarily identical to those of adult mice.
454 For radial measurements, there are small but significant differences between WT and
455 *Cep290* mutant rod cilia (Figure 6I). Centrin measurements were $102 \text{ nm} \pm 28 \text{ nm}$
456 ($n=70$), $87 \text{ nm} \pm 26 \text{ nm}$ ($n=45$), $106 \text{ nm} \pm 28 \text{ nm}$ ($n=20$), and $111 \text{ nm} \pm 29 \text{ nm}$ ($n=30$) for

457 WT, rd16, NN, and KO, respectively, (Figure 6I). There was a small but significant
458 difference between WT and rd16 ($P < .05$, one-way ANOVA with Dunnett's post-hoc
459 analysis). However, we found no significant difference between WT and either NN or
460 KO ($P > .05$). AcTub measurements were $93 \text{ nm} \pm 28 \text{ nm}$ ($n=107$), $107 \text{ nm} \pm 35 \text{ nm}$
461 ($n=90$), $115 \text{ nm} \pm 22 \text{ nm}$ ($n=30$), and $120 \text{ nm} \pm 37 \text{ nm}$ ($n=15$) for WT, rd16, NN, and KO,
462 respectively, (Figure 6I). AcTub was significantly wider in all *Cep290* mutants compared
463 to WT ($P < .001$). Given that TEM results suggest there is a slight contraction of the
464 axonemal radius in CEP290 mutants (see below), the wider appearance of AcTub
465 staining may reflect a greater tendency of the axoneme to flattening in the image plane
466 of the CEP290 mutant retinas.

467 CEP290 measurements were $131 \text{ nm} \pm 38 \text{ nm}$ ($n=135$) and $158 \text{ nm} \pm 51 \text{ nm}$
468 ($n=89$) for WT and rd16, respectively, and CEP290 immunolabeling in rd16 CC was
469 significantly wider than in WT ($P < .005$). CEP290 immunolabeling in NN and KO was not
470 detectable.

471 Similarly, in longitudinal measurements, there were small but significant
472 differences between WT and *Cep290* mutant rod cilia (Figure 6J). Rd16 and KO cilia
473 were significantly shorter than WT when measured with centrin labeling ($P < .001$).
474 However, no difference was found for WT vs. NN ($P > .05$). AcTub labeling appeared
475 slightly shorter in the mutants, however, only the KO cilia achieved statistical
476 significance compared to WT ($P < .001$). CEP290 measurements were $913 \text{ nm} \pm 244 \text{ nm}$
477 ($n=135$) and $750 \text{ nm} \pm 175 \text{ nm}$ ($n=89$) for WT and rd16, respectively, which was
478 significantly shorter than WT ($P < .001$) (Figure 6J). Overall, *Cep290* mutant cilia tended

479 to be wider and shorter compared to age-matched WT cilia. The width differences are
480 consistent with observations by electron microscopy (see below).

481 Because the N-terminus of CEP290 was proposed to interact with the ciliary
482 membrane and was reported to have a slightly wider radial extent than the C-terminus
483 (61, 62), we also used an N-terminal CEP290 antibody to immunolocalize CEP290 in
484 WT animals . The radial width of our N-terminal CEP290 staining was not much wider
485 than the C-terminal CEP290 staining, and the difference was not statistically significant
486 (Supplemental Figure 2). Nonetheless, the resolution of these experiments does not
487 allow us to rule out the possibility of CEP290-membrane interactions *in vivo*.

488 Since the rd16 deletion in CEP290 protein affects the putative microtubule
489 binding domain of CEP290 (56), we asked whether the localization of CEP290 in
490 relation to AcTub is affected in the *Rd16* cilia. The average distances between these
491 antigens in the two genotypes differed from one another by less than the pixel size of 40
492 nm (n=50 for WT, and n=48 for rd16 cilia) and therefore are not reliably resolvable by
493 SIM.

494 *Functional CEP290 is not required for connecting cilium formation.*

495 We next tested the localization of the proposed CEP290 binding partner NPHP5 in mice
496 of different genotypes. *NPHP5/IQCB1* is a causal gene of LCA and Senior Löken
497 syndrome (SLS) (63-65), and LCA and SLS patients with NPHP5 mutations phenocopy
498 *CEP290*-LCA and *CEP290*-SLS cases (55). The C-terminal region of NPHP5 binds to
499 the N-terminal region of CEP290 (66), forming a complex that, through unknown
500 mechanisms, regulates protein trafficking in primary cilia of IMCD3 and hRPE-1 cells
501 (66, 67).

502 We observed NPHP5 localization in the region of the rootlet, basal body, and the
503 base of the CC at P10 in all genotypes (Figure 7A-C). Previous work using a different
504 NPHP5 antibody (64) and different fixation conditions suggested somewhat different
505 patterns of NPHP5 staining, with signal throughout the CC and in the OS (64), or in the
506 proximal OS (68). It was also reported that in NPHP5^{-/-} mice, CEP290 is extensively
507 mislocalized in the ONL and synaptic terminals, a much more dramatic effect than the
508 CEP290 knockout has on NPHP5 localization. Although near or complete loss of
509 CEP290 in our mutant mice results in rapid retinal degeneration and severe phenotypes
510 throughout multiple tissues, nascent photoreceptors in the mutant retina are still able to
511 form cilia with at least a subset of normally localized CC proteins.

512 We also tested the localization of rhodopsin, the visual pigment of the rod
513 photoreceptors, in our mutant mice. Rhodopsin is the most abundant protein in these
514 cells, accounting for up to 90% of total protein in disc membranes of the outer segment
515 (69, 70). We used immunofluorescence with rhodopsin antibodies in retinal sections
516 from P10 NN and KO mice to determine if normal rhodopsin outer segment localization
517 is impaired. While we observed rhodopsin co-localized with cilia at the distal end of
518 nascent photoreceptors in the NN and KO retinas, rhodopsin was also mislocalized in
519 plasma membrane of the IS and the outer nuclear layer in both mutants, as compared
520 to WT retinas (Figure 8). One possible cause could be rhodopsin protein overloading
521 the underdeveloped OS in CEP290-deficient rods. Rhodopsin mislocalization, along
522 with the small changes in radial and longitudinal distribution of CC proteins, are the
523 earliest structural or functional defects yet observed in CEP290 mutant photoreceptors

524 and may be the basis for the later defects in outer segment development and cell
525 survival.

526 *Y-links are present in Cep290 mutant connecting cilia.* Because we could detect
527 connecting cilia by immunofluorescence in developing rods expressing a mutant form of
528 CEP290 at roughly normal levels (*Rd16*), an aberrant form at significantly reduced
529 levels (NN), or no detectable CEP290 (KO), we next asked whether these *Cep290*
530 mutant CC had Y-links. We used TEM to capture longitudinal and cross sections
531 through rod CC from P10 WT, *Rd16*, NN, and KO retinas. In longitudinal TEM images,
532 we found that *Cep290* mutant rods form mostly normal cilia compared to WT cilia
533 (Figure 9A-D), though at reduced numbers in the NN and KO sections. *Rd16* rods
534 formed connecting cilia and rudimentary outer segments (Figure 9B), while NN rods
535 formed rudimentary CC and a small number of nascent outer segment disc-like
536 structures (Figure 9C). We observed almost no disc-like structures in KO TEM sections
537 (Figure 9D). Lower-magnification TEM images of longitudinal sections through the P10
538 *Cep290* mutant retinas displayed overall normal retinal organization outside of the
539 photoreceptor ciliary region in all genotypes (Supplemental Figure 6).

540 In cross sections of the CC, examples from all genotypes have densities that
541 radiate from the microtubule doublets and widen at the ciliary membrane in a manner
542 similar to the Y-links (Figure 9E-H). Although the structures of the CC in the *Cep290*
543 mutants appear grossly normal, we carefully measured the CC dimensions in our TEM
544 cross sections (as depicted schematically below each graph, Figure 9I). We find small
545 contractions of both the axoneme and the ciliary membrane in the mutant CC's (Figure
546 9I). The diameters for the axoneme were 161.3 ± 3.4 nm in KO, 171.6 ± 2.4 nm in NN,

547 and $171.5 \text{ nm} \pm 4.3 \text{ nm}$ in *Rd16* compared to $186 \text{ nm} \pm 2.5 \text{ nm}$ in WT. The diameters for
548 the ciliary membrane were $217.3 \pm 4.4 \text{ nm}$ in KO, $239.7 \text{ nm} \pm 3.1 \text{ nm}$ in NN, and 245.8
549 $\text{nm} \pm 5.2 \text{ nm}$ in *Rd16* compared to $261.1 \text{ nm} \pm 2.4 \text{ nm}$ in WT. Note that we measured
550 diameter in our TEM data by taking two perpendicular radius measurements of cross-
551 sections and used the shortest one in our analysis; this procedure is in contrast to our
552 fluorescence measurements, in which the widths of longitudinal sections are measured;
553 these tend to yield results wider than the actual diameter as the cilia tend to flatten
554 somewhat in the imaging plane. Interestingly, all three mutant retinas displayed Y-link
555 structures in the CC's (Figure 9E-H). Cross-sectional views were difficult to find in the
556 KO, and not all had obvious Y-links, but many did. These results suggest that a fully
557 functional CEP290 is not required to form the Y-links and is not an essential structural
558 component of the Y-links. However, CEP290 may be required for the Y-links to form
559 uniformly throughout the length of the CC, and CEP290 may function indirectly for
560 proper Y-link assembly or stabilization. Additionally, CEP290 in conjunction with the Y-
561 links, may be integral to the structural integrity of the CC, since the distal CC in the KO
562 1) did not usually contain Y-links, 2) did not hold the canonical shape, and 3) did not
563 contain some other CC structures, e.g., the central ring (Supplemental Figure 5).

564

565 **Discussion**

566 The results presented here address the localization of CEP290 and its influence on the
567 localization of other proteins in rod cilia and have important implications for its function
568 and for the mechanisms of disease caused by CEP290 deficiencies. The observation
569 that CEP290 is distributed throughout the length of the rod CC yet is confined to a
570 narrow region of ~200 nm at the base of epithelial cell cilia, suggests its function may
571 also be different in these distinct cell types. Its close association with the axoneme is
572 consistent with another report (62) and with proposals for its contributing to structural
573 connections between microtubules and the membranes, as is the frequently asymmetric
574 distribution of CEP290 with respect to the central axis of the cilium.

575 Based to some extent on lower resolution localization methods, there have been
576 suggestions that what distinguishes the CC from the proximal portions of other cilia is
577 primarily its length - that it could be considered simply a long transition zone. However,
578 this interpretation would be an oversimplification of the multiple unique features of the
579 CC. Whereas CEP290 is located throughout the length of the CC, it is not located
580 throughout the transition zone of other cilia, either in primary cilia, such as the hRPE-1
581 cells studied here and by others (18, 44), or motile cilia, such as those in
582 *Chlamydomonas reinhardtii* (71), but is rather confined to a narrow sub-compartment of
583 the transition zone, and could be considered a component of the distal end of the
584 mother centriole in those cells. Interestingly, in motile cilia of *Paramecium* (72), CEP290
585 was reported to reside in a distal sub-compartment of the transition zone, in close
586 proximity to NPHP8 and TMEM107, but more distal than other TZ components, NPHP4
587 and TMEM216, and to facilitate ciliary shedding induced by Ca²⁺ and ethanol. Centrin

588 are not observed in transition zones of hRPE-1 cell primary cilia (Figure 4), but are
589 found throughout the length of the CC. Some essential CC-resident proteins such as
590 RPGR^{orf15} (73) and RPGRIP1 (74) localize to centrioles in other cell types (75), and
591 others, such as SPATA7 (36), are missing or non-essential in TZ of other cilia. It was
592 recently reported (76) that MKS3/TMEM67, which is considered a marker of the TZ in
593 primary cilia (18, 49, 50) is found at base of and throughout the plasma membrane of
594 rod outer segments, suggesting photoreceptor-specific location and function, which bear
595 further investigation. We show here that the well-characterized TZ marker, NPHP8,
596 locates to a narrow region at the base of the CC, as in other cilia, and not throughout
597 the entire CC length. (Figure 5). Therefore, there may be other unique features and
598 protein complexes within the CC required for photoreceptor function that have yet to be
599 elucidated.

600 In this study, we used two different super resolution imaging techniques - SIM
601 and STORM - to localize CEP290 and other CC proteins within the rod photoreceptor
602 CC of adult mice and young *Cep290* mutant mice. Each of these techniques, along with
603 other superresolution methods such as Stimulated Emission Depletion (STED) (18, 77)
604 microscopy, cryo-electron tomography (26) or immunoelectron microscopy has its
605 advantages, but all are also susceptible to distortions and artifacts, necessitating the
606 use of multiple imaging modalities to reach reliable conclusions. Although we were able
607 to successfully image and measure protein distribution in the CC, SIM and STORM
608 produced slightly different numbers for dimensions of labeled regions in the CC. While
609 both techniques provide better resolution than conventional light microscopy, with
610 STORM providing the better resolution of the two, the discrepancies between the two

611 imaging modes can be attributed in part to different sample preparations and staining
612 protocols; these results highlight a need for continued improvement in microscopy
613 resolution. Advances in correlated light and electron microscopy, immunogold electron
614 microscopy and expansion microscopy (78-81) show promise, as techniques are
615 improved for allowing the preservation and visualization of the ultrastructure while
616 maintaining the antigenicity necessary for immunolabeling.

617 Despite the major disruptions in CC structure and rapid retinal degeneration
618 caused by the CEP290 mutations, their effects on the initial stages of cilium formation
619 and localization of other ciliary proteins appear to be less severe. These results are
620 surprising, given suggestions that CEP290 is essential for ciliogenesis and proposals
621 that it plays a major role in localizing NPHP5 and other transition zone proteins (33, 67,
622 82, 83). They are in stark contrast to those obtained for another LCA-associated protein,
623 SPATA7, deficiencies in which we recently reported to cause drastic redistribution of CC
624 proteins, including CEP290 (36). The idea that CEP290 is essential for ciliogenesis in
625 the retina may have arisen from failure to look at early timepoints in the development of
626 the CC as we have done in this study.

627 Our results are consistent with another proposed role for CEP290, participation in
628 the Y-link structures connecting the axoneme to the ciliary membrane (61). We find that
629 both these Y-links and CEP290 are distributed along the length of the CC. A recent
630 electron tomographic study of primary cilia in epithelial cells (21) demonstrated that their
631 Y-links radiate outward from the microtubule doublets in a narrow proximal portion of
632 the axoneme, well within the 100 nm of CEP290 labeling we observe at the base of the
633 primary cilium in cultured epithelial cells.

634 However, our results are not consistent with the idea that it is a major structural
635 component of the Y-links, as they do form in each mutant, albeit it in a reduced number.
636 This irregular formation of Y-links could contribute to the altered CC dimensions we
637 recorded in *Cep290* mutant rods (Figures 6I-J and 8I). A previous study of a CEP290
638 mutation in *Chlamydomonas reinhardtii* (45) reported a reduction in the number of Y-
639 links, but not obvious abnormalities in structures of those that were present. There were
640 also alterations in the microtubule-to-membrane distances in that mutant, but in that
641 case the distance was increased. All these results support the idea that CEP290 is a
642 component of, or major interactor with, the Y-links and plays an important role in
643 stabilizing the cilium, but CEP290 is not the major Y-shaped structural component
644 bridging the axoneme and ciliary membrane. While we are now able to place additional
645 constraints on CEP290 functions, current evidence suggests it likely has several,
646 including both those common to cilia generally, and those specific for the CC.
647
648

649 **Methods**

650 Animals

651 Wild-type mice used for this study were C57BL/6 aged post-natal day 10 (P10) to 8
652 months. *Rd16* and *Cep290^{tm1.1Jgg}* mice backcrossed to C57BL/6 were acquired from
653 Jackson Laboratory, Bar Harbor, ME (*Rd16*- Stock No: 012283; *Cep290^{tm1.1Jgg}*- Stock
654 No: 013702). *Cep290* KO mice (*Cep290^{tm1A/tm1Asw}*) were acquired from Anand Swaroop
655 at the National Eye Institute, NIH, Bethesda, MD. Details of how these mice were made
656 and genotyping protocols are published (60). Briefly, exons 1–4 of the *Cep290* gene
657 were replaced with a β -gal-neoR cassette by homologous recombination in ES cells,
658 thereby creating a null allele. *Cep290* mutant animals age P10 were used for this study.
659 For immunostaining and immunoblotting, at least three wild type, *Rd16* and
660 *Cep290^{tm1.1Jgg}*, *Cep290^{ko}* mouse replicates were used. Heterozygous *Cep290^{tm1.1Jgg}*
661 crosses were bred to produce *Cep290^{tm1.1Jgg}* mice. Genotyping is described under
662 Supplemental Methods. All procedures were approved by the Baylor College of
663 Medicine Institutional Animal Care and Use Committee and adhered to the Association
664 of Research in Vision and Ophthalmology (ARVO) guidelines for the humane treatment
665 and ethical use of animals for vision research.

666 Cell Culture

667 Human hTERT-RPE-1 (hRPE-1) cells were grown in 50/50 Dulbecco's modified eagle's
668 medium (DMEM)/F12 supplemented with 10% FBS and 10ug Hygromycin B at 37C in a
669 humidified 5% CO₂ atmosphere. To induce ciliation, cells were grown to 70%
670 confluency, split 1:1 in normal growth media on 1.5 coverslips and allowed to settle for

671 12 hours prior to changing to starvation media (DMEM/F12 with 0.5% FBS). Cells
672 remained in starvation media for 36 hours.
673 Cells were fixed with 2% PFA diluted in 1xPBS at room temperature for 10 minutes,
674 blocked in PBSAT (1x PBS with 1% BSA and 0.1% Triton-X100) at room temperature
675 for 30 minutes, incubated with primary antibody in blocking buffer for 45 minutes at
676 room temperature, and secondary antibody in blocking buffer for 30 minutes. Coverslips
677 were mounted with Prolong Glass (Thermo Fisher).

678 Antibodies

679 Details of antibodies used for immunofluorescence staining or immunoblotting are
680 provided in Supplemental Methods.

681 Sample preparation for confocal, deconvolution, and SIM immunofluorescence

682 microscopy

683 Eye cups from mice aged 4-8 months (Figures 2-5) or 10 days postnatal (Figures 6, 7,
684 9) were fixed for five minutes in 1% PFA (Electron Microscopy Science) diluted in 1x
685 PBS, cryopreserved in 30% sucrose overnight at 4C, embedded in Optimal Cutting
686 Temperature (OCT) media, and flash frozen by liquid nitrogen. They were further
687 processed for staining and imaging as described in Supplemental Methods.

688 Deconvolution microscopy and SIM imaging and image analysis

689 For deconvolved wide-field microscopy and SIM, sections were imaged on a
690 DeltaVision OMX Blaze v4 (GE Healthcare) equipped with 405 nm, 488 nm, 568 nm,
691 647 nm lasers and a BGR filter drawer, a PLANPON6 60x / NA 1.42 (Olympus) using oil
692 with a refractive index of 1.520, and front illuminated Edge sCMOS (PCO). For SIM, a
693 total of 15 images were acquired per section per channel at a z-spacing of 125 nm.

694 Deconvolved images were acquired in conventional mode, while SIM images were
695 acquired in SI mode. Reconstructions were performed in Softworx 7 software.

696 Deconvolved images were deconvolved and aligned, and SIM images were
697 reconstructed using SI reconstruction and OMX alignment. Default deconvolve and
698 reconstruction settings were used. After analysis, reconstructions were processed in
699 Fiji/ImageJ, and the Straighten tool was applied to straighten curved or bent cilia to
700 acquire accurate profiles. ROI's of digitally straightened deconvolved and STORM
701 reconstructions were measured using row-average profiling, which plots the average
702 intensity across the width of the ROI for each row of pixels along the length of the ROI.
703 Pixels were converted to nm for accurate scaling. From these row-average profiles, the
704 edges of antibody labeling in SIM were set as 33% of the maximum intensity value for
705 connecting cilia and FWHM for hRPE-1 primary cilia, and radius was measured as the
706 maximum intensity value for either acetylated α -tubulin (AcTub) and centrin to 33%
707 maximum labeling for the protein of interest. All measurements were made in a 1.1 μm
708 longitudinal region just above the basal body that corresponds to the length of the
709 ultrastructural connecting cilium and provided as mean \pm standard deviation. For radius
710 measurements using SIM images, signals that extended beyond either the AcTub or
711 centrin labeling were measured. All measurements were rounded to the nearest
712 nanometer. Measurements were not collected for deconvolved images, due to its poor
713 resolution in the focal plane.

714 Transmission electron microscopy (TEM)

715 Adult mice were euthanized by CO₂ asphyxiation followed by decapitation. Eye globes
716 were enucleated and fixed in 0.1M sodium cacodylate buffer (pH 7.2) containing 2.5%

717 glutaraldehyde at room temperature for 10 minutes. Cornea and lens were removed
718 from the globe and the fixation of the remaining eye cup continued for 2 hours. After
719 rinsing in buffer, the eye cups were post-fixed and heavy metal-contrasted with
720 potassium ferrocyanide, osmium tetroxide, thiocarbohydrazide, uranyl acetate and lead
721 aspartate. Next, the eye cups were dehydrated in acetone and embedded in Embed
722 812 resin. Serial block-face imaging of the resin blocks was performed on a scanning
723 electron microscope (SEM; Mira 3, Tescan) equipped with an in chamber
724 ultramicrotome (3View, Gatan). Serial images of the sectioned block-face (200 nm
725 between sections) were observed on a digital monitor until the tissue plane was reached
726 containing the outer segment- connecting cilium interface of the photoreceptors. The
727 sectioned block was then removed from the SEM and placed in a conventional
728 ultramicrotome for routine sectioning (80-100nm thin) and collection on copper grids
729 (200 mesh) for imaging on the transmission electron microscope (Tecnai 12, FEI).
730 Optimal cross-sectional images of the cilia were achieved using a goniometer specimen
731 chamber capable of ± 60 -degree tilting in conjunction with a motorized rotating (360
732 degree) specimen holder.

733 For P10 studies, mice were euthanized by CO₂ asphyxiation followed by decapitation at
734 P10. Eyes were enucleated, the cornea and lens were removed, and eye globes were
735 placed in fixative (2% paraformaldehyde, 2% glutaraldehyde, 3.4mM CaCl₂ in 0.2M
736 HEPES, pH 7.4) for 24 hours, rocking at room temperature. The eyecups were then
737 washed in 1X PBS for 5 minutes, placed in 4% agarose, and left to polymerize for 30
738 minutes at 4C. 150 μ m sections were cut on a vibratome and subsequently stained with
739 1% Tannic Acid with 0.5% Saponin in 0.1M HEPES, pH 7.4 for 1 hour, rocking at room

740 temperature. After rinsing in MilliQ water, the sections were then stained with 1% uranyl
741 acetate in 0.2M Maleate Buffer, pH 6.0 for 1 hour, rocking at room temperature. The
742 sections were rinsed in MilliQ water and dehydrated in a series of ethanol washes (50%,
743 70%, 90%, 100%x2) for 15 minutes each, followed by infiltration Ultra Bed Epoxy Resin.
744 The sections were embedded in resin between two ACLAR sheets sandwiched between
745 glass slides in a 60C oven for 48 hours. At 24 hours, the top slide and ACLAR sheet
746 was removed and resin blocks in BEEM[®] capsules were stamped onto each section to
747 allow for polymerization the following 24 hours. Ultrathin silver sections were placed on
748 copper grids and post-stained in 1.2% uranyl acetate in MilliQ water for 6 minutes,
749 followed by staining in Sato's Lead for 2 minutes. Sections were imaged on a Hitachi
750 H7500 or a JOEL JEM-1400 electron microscope. Measurements from radial cross
751 sections of photoreceptor CC were performed on Image J. Since the cross sections
752 were not perfectly circular, two intersecting measurements (along the shortest and
753 longest axes) were taken and the shortest measurement was used in the analysis for
754 Figure 9I.

755 STORM immunohistochemistry and resin embedding

756 Retinas from 6-8 week old WT mice were immunolabeled for STORM using a protocol
757 we developed previously (Robichaux et al 2019). Details are provided in Supplemental
758 Methods.

759 STORM image acquisition

760 Immediately prior to imaging, 10% sodium hydroxide (w/v) was mixed with pure 200-
761 proof ethanol for 45 minutes to prepare a mild sodium ethoxide solution. Glass-bottom
762 dishes with ultra-thin retina sections were immersed for 30-45 minutes for chemical

763 etching of the resin. Etched sections were then washed and dried on a 50°C heat block.
764 The following STORM imaging buffer was prepared: 45 mM Tris (pH 8.0), 9 mM NaCl,
765 oxygen scavenging system: 0.7 mg•ml⁻¹ glucose oxidase (Amresco) + 42.5 µg ml⁻¹
766 catalase (Sigma), 10% (w/v) glucose + 100 mM MEA (i.e. L-cysteamine, Chem-Impex) +
767 10% VECTASHIELD (Vector Laboratories). Imaging buffer was added onto the dried,
768 etched sections and sealed with a second number 1.5 coverslip for imaging.

769 Imaging was performed on the Nikon N-STORM system, which features a CFI Apo
770 TIRF 100x oil objective (NA1.49) on an inverted Nikon Ti Eclipse microscope. STORM
771 image acquisition was controlled by NIS-Elements Ar software.

772 To begin a STORM acquisition, both the 561 nm and 647 nm laser lines were increased
773 to maximum power to photobleach the fluorescence and initiate photoswitching.

774 Imaging frames were collected at ~56 frames per second. 50,000 frames were collected
775 for each imaging experiment.

776 STORM image analysis

777 2D-STORM Analysis of STORM acquisition frames was performed using NIS Elements
778 Ar Analysis software. Analysis identification settings were used for detection of the
779 individual point spread function (PSF) of photoswitching events in frames from both
780 channels to be accepted and reconstructed as 2D Gaussian data points. These settings
781 were as follows: Minimum PSF height: 400, Maximum PSF height: 65,636, Minimum
782 PSF Width: 200 nm, Maximum PSF Width: 700 nm, Initial Fit Width: 350 nm, Maximum
783 Axial Ratio: 2.5, Maximum Displacement: 1 pixel.

784 After analysis, reconstructions were processed in Fiji/ImageJ using the similar method
785 described to analyze SIM reconstructions. The edges of STORM clusters were set as
786 $1/e$ the maximum intensity value instead of $1/2$ the maximum intensity.

787 Immunoblotting

788 P10 retinas were collected in 2x protease inhibitor (Roche) diluted in 1x PBS (6.7mM
789 PO_4 with Ca^{++} and Mg^{++}) (Hyclone) from WT *Rd16*, NN, and KO animals, sonicated in
790 1x SDS sample buffer (250mM Tris pH 6.8, 10% SDS, 30% glycerol, 5% β -
791 mercaptoethanol), and 1 retina per lane was loaded on a 3-8% Tris-Acetate gel for
792 SDS-PAGE. Gels were ran in 1x Tris-Acetate SDS Running Buffer (20X: 50mM Tricine,
793 50mM Tris Base, 0.1% SDS, pH 8.24; Bio-Rad). Proteins were transferred to
794 unsupported nitrocellulose membranes in 1x Tris-Acetate transfer buffer (20X: 25mM
795 Bicine, 25mM Bis-Tris (free base), 1mM EDTA, pH 7.2; Bio-Rad) overnight at RT.
796 Membrane was blocked in 5% skim milk for 1 hour at room temperature. Primary
797 antibodies were added and incubated overnight in 5% non-fat dry milk at 4°C.
798 Secondary HRP antibodies (LI-COR Biosciences) were incubated with the membranes
799 for 2 hours with shaking at room temperature. Membranes were imaged on an Azure
800 Scanner with a 20-90s exposure time. Image processing was performed in Adobe
801 Photoshop. All image contrast adjustments were applied identically to all images being
802 compared.

803 Statistics

804 Numbers of animals and/or replicates are indicated in each figure legend. Two-way
805 comparisons between antigens in one genotype were analyzed by Student's *t*-test.

806 Multiple comparisons were analyzed by one-way Anova with Tukey's or Dunnett's post-
807 hoc correction for multiple comparisons.

808 Study Approval.

809 All animal studies were approved by the Baylor College of Medicine Institutional Animal
810 Care and Use Committee. They adhered to the Association of Research in Vision and
811 Ophthalmology (ARVO) guidelines for the humane treatment and ethical use of animals
812 for vision research.

813

814

815 **Author Contributions**

816 VEP designed and executed experiments, analyzed data and wrote the manuscript. She
817 was assigned first authorship for initiating the project and writing the initial manuscript.
818 ARM and MAR designed and executed experiments, analyzed data, wrote sections of
819 the manuscript and helped edit it. TGW supervised the project, analyzed data and
820 helped edit the manuscript.

821 **Acknowledgements**

822 We thank Melina A Agosto for technical assistance and comments on the manuscript;
823 Michael Mancini, Fabio Stossi, Christopher Hampton, and Hannah Johnson of Baylor
824 College of Medicine Integrated Microscopy Core (IMC) for technical support and advice,
825 Lita Duraine of Baylor College of Medicine Dan and Jan Duncan Neurological Research
826 Institute for assistance with additional TEM imaging, and Alan Burns, Samuel Hanlon,
827 and Margaret Gondo of the University of Houston School of Optometry for serial-
828 sectioning SEM and TEM.

829 **Funding Sources**

830 This work was supported by NIH grants R01-EY07981 (TGW) , R01-EY26545 (TGW),
831 F32-EY027171 (MAR), T32-EY007102 (ARM), F32-EY031574 (ARM), F31-EY028025
832 (VLP), S10-OD020151 (MM), and P30 EY007551 (AB).
833

834

835 References

- 836 1. Badano JL, et al. The ciliopathies: an emerging class of human genetic disorders. *Annu*
837 *Rev Genomics Hum Genet.* 2006;7:125-48.
- 838 2. Zariwala MA, Knowles MR, and Omran H. Genetic defects in ciliary structure and
839 function. *Annu Rev Physiol.* 2007;69:423-50.
- 840 3. Bujakowska KM, Liu Q, and Pierce EA. Photoreceptor Cilia and Retinal Ciliopathies. *Cold*
841 *Spring Harb Perspect Biol.* 2017.
- 842 4. Weleber RG et al. eds. *GeneReviews((R))*. Seattle (WA); 1993.
- 843 5. den Hollander AI et al. Mutations in the CEP290 (NPHP6) gene are a frequent cause of
844 Leber congenital amaurosis. *Am J Hum Genet.* 2006;79(3):556-61.
- 845 6. den Hollander AI et al. Leber congenital amaurosis: genes, proteins and disease
846 mechanisms. *Prog Retin Eye Res.* 2008;27(4):391-419.
- 847 7. Perrault I et al. Spectrum of NPHP6/CEP290 mutations in Leber congenital amaurosis
848 and delineation of the associated phenotype. *Hum Mutat.* 2007;28(4):416.
- 849 8. Birtel J, et al. Next-generation sequencing identifies unexpected genotype-phenotype
850 correlations in patients with retinitis pigmentosa. *PLoS One.* 2018;13(12):e0207958.
- 851 9. Valente EM et al. Mutations in CEP290, which encodes a centrosomal protein, cause
852 pleiotropic forms of Joubert syndrome. *Nat Genet.* 2006;38(6):623-5.
- 853 10. Baala L, et al. Pleiotropic effects of CEP290 (NPHP6) mutations extend to Meckel
854 syndrome. *Am J Hum Genet.* 2007;81(1):170-9.
- 855 11. Brancati F, et al. CEP290 mutations are frequently identified in the oculo-renal form of
856 Joubert syndrome-related disorders. *Am J Hum Genet.* 2007;81(1):104-13.
- 857 12. Frank V et al. Mutations of the CEP290 gene encoding a centrosomal protein cause
858 Meckel-Gruber syndrome. *Hum Mutat.* 2008;29(1):45-52.
- 859 13. Leitch CC et al. Hypomorphic mutations in syndromic encephalocele genes are
860 associated with Bardet-Biedl syndrome. *Nat Genet.* 2008;40(4):443-8.
- 861 14. Coppieters F et al. CEP290, a gene with many faces: mutation overview and
862 presentation of CEP290base. *Hum Mutat.* 2010;31(10):1097-108.
- 863 15. Pazour GJ, and Witman GB. The vertebrate primary cilium is a sensory organelle. *Curr*
864 *Opin Cell Biol.* 2003;15(1):105-10.
- 865 16. Satir P, and Christensen ST. Overview of structure and function of mammalian cilia.
866 *Annu Rev Physiol.* 2007;69:377-400.
- 867 17. Singla V, and Reiter JF. The primary cilium as the cell's antenna: signaling at a sensory
868 organelle. *Science.* 2006;313(5787):629-33.
- 869 18. Yang TT, Su J, Wang WJ, Craige B, Witman GB, Tsou MF, et al. Superresolution Pattern
870 Recognition Reveals the Architectural Map of the Ciliary Transition Zone. *Sci Rep.*
871 2015;5:14096.
- 872 19. Ringo DL. Flagellar motion and fine structure of the flagellar apparatus in
873 Chlamydomonas. *J Cell Biol.* 1967;33(3):543-71.
- 874 20. Gilula NB, and Satir P. The ciliary necklace. A ciliary membrane specialization. *J Cell Biol.*
875 1972;53(2):494-509.
- 876 21. Sun S et al. Three-dimensional architecture of epithelial primary cilia. *Proc Natl Acad Sci*
877 *U S A.* 2019;116(19):9370-9.

- 878 22. Robichaux MA et al. Defining the layers of a sensory cilium with STORM and
879 cryoelectron nanoscopy. *Proc Natl Acad Sci U S A*. 2019;116(47):23562-72.
- 880 23. Pazour GJ, et al. Polycystin-2 localizes to kidney cilia and the ciliary level is elevated in
881 orpk mice with polycystic kidney disease. *Curr Biol*. 2002;12(11):R378-80.
- 882 24. Handel M et al. Selective targeting of somatostatin receptor 3 to neuronal cilia.
883 *Neuroscience*. 1999;89(3):909-26.
- 884 25. Wensel TG et al. Structure and dynamics of photoreceptor sensory cilia. *Pflugers Arch*.
885 2021.
- 886 26. Gilliam JC et al. Three-dimensional architecture of the rod sensory cilium and its
887 disruption in retinal neurodegeneration. *Cell*. 2012;151(5):1029-41.
- 888 27. Salisbury JL. Centrin, centrosomes, and mitotic spindle poles. *Curr Opin Cell Biol*.
889 1995;7(1):39-45.
- 890 28. Wolfrum U. Centrin in the photoreceptor cells of mammalian retinae. *Cell Motil*
891 *Cytoskeleton*. 1995;32(1):55-64.
- 892 29. Wolfrum U, and Salisbury JL. Expression of centrin isoforms in the mammalian retina.
893 *Exp Cell Res*. 1998;242(1):10-7.
- 894 30. Laoukili J et al. Differential expression and cellular distribution of centrin isoforms during
895 human ciliated cell differentiation in vitro. *J Cell Sci*. 2000;113 (Pt 8):1355-64.
- 896 31. Pulvermuller A et al. Calcium-dependent assembly of centrin-G-protein complex in
897 photoreceptor cells. *Mol Cell Biol*. 2002;22(7):2194-203.
- 898 32. Muresan V, and Besharse JC. Complex intermolecular interactions maintain a stable
899 linkage between the photoreceptor connecting cilium axoneme and plasma membrane.
900 *Cell Motil Cytoskeleton*. 1994;28(3):213-30.
- 901 33. Kim J, Krishnaswami SR, and Gleeson JG. CEP290 interacts with the centriolar satellite
902 component PCM-1 and is required for Rab8 localization to the primary cilium. *Hum Mol*
903 *Genet*. 2008;17(23):3796-805.
- 904 34. Tsang WY et al. CP110 suppresses primary cilia formation through its interaction with
905 CEP290, a protein deficient in human ciliary disease. *Dev Cell*. 2008;15(2):187-97.
- 906 35. Garcia-Gonzalo FR et al. A transition zone complex regulates mammalian ciliogenesis
907 and ciliary membrane composition. *Nat Genet*. 2011;43(8):776-84.
- 908 36. Dharmat R et al. SPATA7 maintains a novel photoreceptor-specific zone in the distal
909 connecting cilium. *J Cell Biol*. 2018;217(8):2851-65.
- 910 37. Cox G, and Sheppard CJ. Practical limits of resolution in confocal and non-linear
911 microscopy. *Microsc Res Tech*. 2004;63(1):18-22.
- 912 38. Gustafsson MG. Surpassing the lateral resolution limit by a factor of two using
913 structured illumination microscopy. *J Microsc*. 2000;198(Pt 2):82-7.
- 914 39. Kim D, Deerinck TJ et al. Correlative stochastic optical reconstruction microscopy and
915 electron microscopy. *PLoS One*. 2015;10(4):e0124581.
- 916 40. Graser S et al. Cep164, a novel centriole appendage protein required for primary cilium
917 formation. *J Cell Biol*. 2007;179(2):321-30.
- 918 41. Acu ID et al. Coordination of centrosome homeostasis and DNA repair is intact in MCF-7
919 and disrupted in MDA-MB 231 breast cancer cells. *Cancer Res*. 2010;70(8):3320-8.

- 920 42. Piperno G, and Fuller MT. Monoclonal antibodies specific for an acetylated form of
921 alpha-tubulin recognize the antigen in cilia and flagella from a variety of organisms. *J*
922 *Cell Biol.* 1985;101(6):2085-94.
- 923 43. Molday RS, and Molday LL. Identification and characterization of multiple forms of
924 rhodopsin and minor proteins in frog and bovine rod outer segment disc membranes.
925 Electrophoresis, lectin labeling, and proteolysis studies. *J Biol Chem.* 1979;254(11):4653-
926 60.
- 927 44. Yang TT et al. Super-resolution architecture of mammalian centriole distal appendages
928 reveals distinct blade and matrix functional components. *Nat Commun.* 2018;9(1):2023.
- 929 45. Craige B et al. CEP290 tethers flagellar transition zone microtubules to the membrane
930 and regulates flagellar protein content. *J Cell Biol.* 2010;190(5):927-40.
- 931 46. Horst CJ, Forestner DM, and Besharse JC. Cytoskeletal-membrane interactions: a stable
932 interaction between cell surface glycoconjugates and doublet microtubules of the
933 photoreceptor connecting cilium. *J Cell Biol.* 1987;105(6 Pt 2):2973-87.
- 934 47. Tokuyasu K, and Yamada E. The fine structure of the retina studied with the electron
935 microscope. IV. Morphogenesis of outer segments of retinal rods. *J Biophys Biochem*
936 *Cytol.* 1959;6:225-30.
- 937 48. Rohlich P. The sensory cilium of retinal rods is analogous to the transitional zone of
938 motile cilia. *Cell Tissue Res.* 1975;161(3):421-30.
- 939 49. Dawe HR et al. The Meckel-Gruber Syndrome proteins MKS1 and meckelin interact and
940 are required for primary cilium formation. *Hum Mol Genet.* 2007;16(2):173-86.
- 941 50. Tiwari S et al. Meckelin 3 is necessary for photoreceptor outer segment development in
942 rat Meckel syndrome. *PLoS ONE.* 2013;8(3):e59306.
- 943 51. Williams CL et al. MKS and NPHP modules cooperate to establish basal body/transition
944 zone membrane associations and ciliary gate function during ciliogenesis. *J Cell Biol.*
945 2011;192(6):1023-41.
- 946 52. Gerhardt C et al. The transition zone protein Rpgrip1l regulates proteasomal activity at
947 the primary cilium. *J Cell Biol.* 2015;210(1):115-33.
- 948 53. Hong DH et al. A retinitis pigmentosa GTPase regulator (RPGR)-deficient mouse model
949 for X-linked retinitis pigmentosa (RP3). *Proc Natl Acad Sci U S A.* 2000;97(7):3649-54.
- 950 54. Chang B. Mouse Models as Tools to Identify Genetic Pathways for Retinal Degeneration,
951 as Exemplified by Leber's Congenital Amaurosis. *Methods Mol Biol.* 2016;1438:417-30.
- 952 55. Cideciyan AV et al. Cone photoreceptors are the main targets for gene therapy of NPHP5
953 (IQCB1) or NPHP6 (CEP290) blindness: generation of an all-cone Nphp6 hypomorph
954 mouse that mimics the human retinal ciliopathy. *Hum Mol Genet.* 2011;20(7):1411-23.
- 955 56. Chang B et al. In-frame deletion in a novel centrosomal/ciliary protein CEP290/NPHP6
956 perturbs its interaction with RPGR and results in early-onset retinal degeneration in the
957 rd16 mouse. *Hum Mol Genet.* 2006;15(11):1847-57.
- 958 57. Lancaster MA et al. Defective Wnt-dependent cerebellar midline fusion in a mouse
959 model of Joubert syndrome. *Nat Med.* 2011;17(6):726-31.
- 960 58. Hynes AM et al. Murine Joubert syndrome reveals Hedgehog signaling defects as a
961 potential therapeutic target for nephronophthisis. *Proc Natl Acad Sci U S A.*
962 2014;111(27):9893-8.

- 963 59. Datta P et al. CEP290 myosin-tail homology domain is essential for protein confinement
964 between inner and outer segments in photoreceptors. 2019.
- 965 60. Rachel RA et al. CEP290 alleles in mice disrupt tissue-specific cilia biogenesis and
966 recapitulate features of syndromic ciliopathies. *Hum Mol Genet.* 2015;24(13):3775-91.
- 967 61. Drivas TG, Holzbaaur EL, and Bennett J. Disruption of CEP290 microtubule/membrane-
968 binding domains causes retinal degeneration. *J Clin Invest.* 2013;123(10):4525-39.
- 969 62. Jana SC et al. Differential regulation of transition zone and centriole proteins contributes
970 to ciliary base diversity. *Nat Cell Biol.* 2018;20(8):928-41.
- 971 63. Stone EM et al. Variations in NPHP5 in patients with nonsyndromic leber congenital
972 amaurosis and Senior-Loken syndrome. *Arch Ophthalmol.* 2011;129(1):81-7.
- 973 64. Otto EA et al. Nephrocystin-5, a ciliary IQ domain protein, is mutated in Senior-Loken
974 syndrome and interacts with RPGR and calmodulin. *Nat Genet.* 2005;37(3):282-8.
- 975 65. Estrada-Cuzcano A et al. IQCB1 mutations in patients with leber congenital amaurosis.
976 *Invest Ophthalmol Vis Sci.* 2011;52(2):834-9.
- 977 66. Barbelanne M et al. Pathogenic NPHP5 mutations impair protein interaction with
978 Cep290, a prerequisite for ciliogenesis. *Hum Mol Genet.* 2013;22(12):2482-94.
- 979 67. Barbelanne M et al. Nephrocystin proteins NPHP5 and Cep290 regulate BBSome
980 integrity, ciliary trafficking and cargo delivery. *Hum Mol Genet.* 2015;24(8):2185-200.
- 981 68. Ronquillo CC et al. Ciliopathy-associated IQCB1/NPHP5 protein is required for mouse
982 photoreceptor outer segment formation. *FASEB J.* 2016;30(10):3400-12.
- 983 69. Basinger S, Bok D, and Hall M. Rhodopsin in the rod outer segment plasma membrane. *J*
984 *Cell Biol.* 1976;69(1):29-42.
- 985 70. Heitzmann H. Rhodopsin is the predominant protein of rod outer segment membranes.
986 *Nat New Biol.* 1972;235(56):114.
- 987 71. Awata J et al. NPHP4 controls ciliary trafficking of membrane proteins and large soluble
988 proteins at the transition zone. *J Cell Sci.* 2014;127(Pt 21):4714-27.
- 989 72. Gogendeau D et al. MKS-NPHP module proteins control ciliary shedding at the transition
990 zone. *PLoS Biol.* 2020;18(3):e3000640.
- 991 73. Megaw RD, Soares DC, and Wright AF. RPGR: Its role in photoreceptor physiology,
992 human disease, and future therapies. *Exp Eye Res.* 2015;138:32-41.
- 993 74. Li T. Leber congenital amaurosis caused by mutations in RPGRIP1. *Cold Spring Harbor*
994 *perspectives in medicine.* 2014;5(4).
- 995 75. Shu X et al. RPGR ORF15 isoform co-localizes with RPGRIP1 at centrioles and basal
996 bodies and interacts with nucleophosmin. *Hum Mol Genet.* 2005;14(9):1183-97.
- 997 76. Skiba NP et al. TMEM67, TMEM237, and Embigin in Complex With Monocarboxylate
998 Transporter MCT1 Are Unique Components of the Photoreceptor Outer Segment Plasma
999 Membrane. *Mol Cell Proteomics.* 2021;20:100088.
- 1000 77. Lau L et al. STED microscopy with optimized labeling density reveals 9-fold arrangement
1001 of a centriole protein. *Biophys J.* 2012;102(12):2926-35.
- 1002 78. Tillberg PW et al. Protein-retention expansion microscopy of cells and tissues labeled
1003 using standard fluorescent proteins and antibodies. *Nat Biotechnol.* 2016;34(9):987-92.
- 1004 79. Chang JB et al. Iterative expansion microscopy. *Nat Methods.* 2017;14(6):593-9.
- 1005 80. Macaluso FP et al.. CLEM Methods for Studying Primary Cilia. *Methods Mol Biol.*
1006 2016;1454:193-202.

- 1007 81. Norris RP, Baena V, and Terasaki M. Localization of phosphorylated connexin 43 using
1008 serial section immunogold electron microscopy. *J Cell Sci.* 2017;130(7):1333-40.
- 1009 82. Lopes CA et al. Centriolar satellites are assembly points for proteins implicated in human
1010 ciliopathies, including oral-facial-digital syndrome 1. *J Cell Sci.* 2011;124(Pt 4):600-12.
- 1011 83. Stowe TR et al. The centriolar satellite proteins Cep72 and Cep290 interact and are
1012 required for recruitment of BBS proteins to the cilium. *Mol Biol Cell.* 2012;23(17):3322-
1013 35.
- 1014
- 1015

1016 **Figure Legends**

1017

1018 **Figure 1. The photoreceptor connecting cilium.** (A) The photoreceptors are the most
1019 posterior cells in the neural retina at the back of the eye. (B) Rod photoreceptor cells
1020 are distributed across four layers of the retina. (C) The connecting cilium links the outer
1021 segment to the inner segment. The dashed link shows the portion of the connecting
1022 cilium in the cross-sectional view. The dimensions of the connecting cilium are ~1100
1023 nm by 300 nm. OS, outer segment; IS, inner segment; ONL, outer nuclear layer; OPL,
1024 outer plexiform layer; CC, connecting cilium; BB, basal body; TF, transition fibers; MT,
1025 microtubule doublets.

1026

1027 **Figure 2. CEP290 localizes throughout the length of the CC and in close proximity**
1028 **to the microtubule doublets.** (A-B) SIM and STORM images of representative cilia
1029 from adult retina, immunostained for transition fiber protein CEP164 and axonemal
1030 lumen protein, Centrin (A) or CEP164 and CEP290 (B). Row average intensity plots are
1031 shown. (C) SIM image of a representative cross section through the CC with separated
1032 channels to the right. The white line depicts the position of the average intensity line
1033 plot. (D-F) SIM and STORM longitudinal images of representative cilia immunostained
1034 for CEP290 and acetylated- α -tubulin (AcTub, E) or glycocalyx label WGA (F). Row-
1035 average intensity plots are shown. For CEP290/WGA labelled cilia, high and low
1036 magnification widefield Tuba1 antibody staining (green) overlay is shown. (G) Dot plot
1037 with averages and standard deviations of the lengths of CEP290 and centrin staining in
1038 the CC for SIM and STORM. (H) Dot plot with averages and standard deviations of the

1039 radii of CEP290, AcTub, and centrin in the CC for SIM and STORM. 33% of the
1040 maximum intensity value of each channel was used as the boundary criterion for the
1041 measurement of each cilium. Measurements were compared with Student's t-test and
1042 one-way ANOVA and Tukey's post-hoc test, respectively. (I) A color-coded schematic of
1043 a CC. AcTub, acetylated α -tubulin; WGA, wheat germ agglutinin; CC, connecting cilium.
1044 Scale bar 200 nm. Dotted line indicates CC/OS border. Measurements were from three
1045 different animals and SIM images of 75 cilia for CEP290, 30 for AcTub and 45 for
1046 centrin, or STORM images of 42 cilia from six animals for CEP290, 16 cilia from three
1047 animals for AcTub and 52 cilia from three animals for centrin.

1048

1049 **Figure 3. Y-links appear throughout the CC.** (A, B) TEM image depicting the OS/ CC
1050 interface. CC (white arrow), discs *en face* (star), and cilium and discs (yellow asterisks)
1051 from photoreceptors are shown, with MT doublets connected to Y-links outlined in
1052 yellow boxes. Scale bar 200 nm. (C, D) CC from neighboring photoreceptor cells. Y-
1053 links (yellow boxes) are visible. Scale bar 50 nm. (E, F) Image of cilium and discs (white
1054 asterisk) from another photoreceptor cell. Y-links (yellow box) are visible. Scale bar 100
1055 nm; Inset (G) scale bar 50 nm. CC, connecting cilium; OS, outer segment.

1056

1057 **Figure 4. CEP290 localizes to the base of the primary cilium in epithelial cells.** (A-
1058 D) SIM images of a representative centriole and cilium for each labeling condition,
1059 CEP290, CEP164, NPHP8, and MKS3, respectively, with centrin as a marker for the
1060 BB, and AcTub as marker for the axoneme. Row-average intensity plots are below each
1061 image. (E-F) Dot plot with average and standard deviation of the length distal to centrin

1062 (illustrated in intensity plot of A) or the length proximal to AcTub (illustrated in intensity
1063 plot of B). 33% of the maximum intensity value of each channel was used as the
1064 boundary criterion for the measurement of each cilium. Measurements were compared
1065 with one-way ANOVA and Dunnett's post-hoc test. G) A color-coded schematic of a
1066 primary cilium with results shown. AcTub, acetylated α -tubulin.

1067

1068 **Figure 5. Comparison of ciliary protein localization in RPE and photoreceptor**
1069 **cilia.** (A-B) SIM images depicting CEP290 and NPHP8 localization in RPE and
1070 photoreceptor cilia. Row average intensity plots are below each image. (C) A color-
1071 coded schematic of a primary cilium in RPE and photoreceptor with results shown.
1072 AcTub, acetylated α -tubulin. See also Supplemental Figure 4.

1073

1074 **Figure 6. CC develops in *Cep290* mutant prior to degeneration.** (A-H) SIM images
1075 (high magnification, right; low magnification, left) of cilia from P10 WT, rd16, NN, and
1076 KO animals labelled with CEP290, AcTub, and centrin. Scale bar on left, 1 μ m. SIM
1077 (right) images of representative cilia. Row-average intensity and column average
1078 intensity plots are shown. AcTub and centrin gains were adjusted to subsaturation for
1079 image presentation. CEP290 intensity levels in *Cep290* mutants were normalized to wild
1080 type levels (I-J) Dot plots with averages and standard deviations of the maximum radii
1081 and lengths of CEP290, AcTub, and centrin in the cilium. Cilia were imaged from three
1082 non-littermate mice for each genotype. 33% of the maximum intensity value of each
1083 channel was used as the boundary criterion for the measurement of each cilium.
1084 Measurements were compared with one-way ANOVA and Dunnett's post-hoc test. (K)

1085 Western blots demonstrating detection of CEP290 protein products. Expected sizes for
1086 WT CEP290, CEP290(rd16), and AcTub are 290kDa, 270 kDa and 50 kDa,
1087 respectively. *Asterisk indicates band shift in the rd16 protein product. Dotted line
1088 indicates CC/OS border. AcTub, acetylated α -tubulin; CC, connecting cilium; WT, wild
1089 type; rd16, *Cep290^{rd16}*; nn, near null-*Cep290^{tm1.1Jgg}*; ko, knockout-*Cep290*; ND, not
1090 detectable. The N-terminal blot lanes were run simultaneously on the same samples as
1091 the C-terminal blot.

1092

1093 **Figure 7. NPHP5 localization in WT and in *Cep290* mutants.** NPHP5 antibody signal
1094 localizes to the base of the CC and the region on the rootlet and BB in WT and in
1095 *Cep290* mutant animals before photoreceptor degeneration. Confocal images of P10
1096 WT (A), rd16 (B), NN (C), and KO (D) cilia with separated channels at low magnification
1097 to the right. WT image acquisition and processing settings were applied to WT, rd16,
1098 nn, and KO data. Scale bar 10 μ m. AcTub, acetylated α -tubulin; CC, connecting cilium;
1099 WT, wild type; rd16, *Cep290^{rd16}*; nn, near null-*Cep290^{tm1.1Jgg}*; ko, knockout-*Cep290*.

1100

1101

1102 **Figure 8. Rhodopsin localization in P10 *Cep290* mutant cilia.** Confocal images of
1103 retina from P10 WT, NN, and KO stained for rhodopsin (green) and DAPI (nuclear stain,
1104 blue). Acquisition settings and image processing were identical for all samples. OS,
1105 outer segment; IS, inner segment; ONL, outer nuclear layer; INL, inner nuclear layer;
1106 WT, wild type; rd16, *Cep290^{rd16}*; nn, near null-*Cep290^{tm1.1Jgg}*; ko, knockout-*Cep290*.
1107 Scale bar 20 μ m. Bottom panel shows integrated intensities for each layer normalized by
1108 total rhodopsin signal for the images above.

1109

1110 **Figure 9. Y-links are present in P10 *Cep290* mutant CC.** (A-C) TEM longitudinal
1111 images of P10 photoreceptor cilia from (A) WT, (B) *Rd16*, and (C) NN, and (D) KO
1112 animals depicting the (A) properly developed CC and OS, (B) rudimentary OS, and (C,
1113 D) rudimentary CC. CC (yellow arrow) and OS discs (yellow asterisk) are highlighted.
1114 Scale bar 2 μ m. (E-H) Cross section images through the CC of (E) WT, (F) *Rd16*, (G)
1115 NN, and (H) KO animals. Y-links (yellow box) are visible in WT and *Cep290* mutants.
1116 Scale bar 100 nm. Insets highlight Y-links within the box. Scale bar 20nm. Lower
1117 magnification views of the same regions of these retinas are shown in Supplemental
1118 Figure 6. (I) Cross sections through distal ends of CC showing abnormal structures in
1119 KO retinas. See also Supplemental Figure 5B. (J) Dot plot with averages and SEMs of
1120 measurements of annotated areas within connecting cilium sections from WT (43 cilia
1121 from 2 animals), *Rd16* (29 cilia from 3 animals), NN (58 cilia from two animals), and KO
1122 (44 cilia from 2 animals). Measurements were compared using one-way ANOVA with
1123 Dunnett's test.

1124

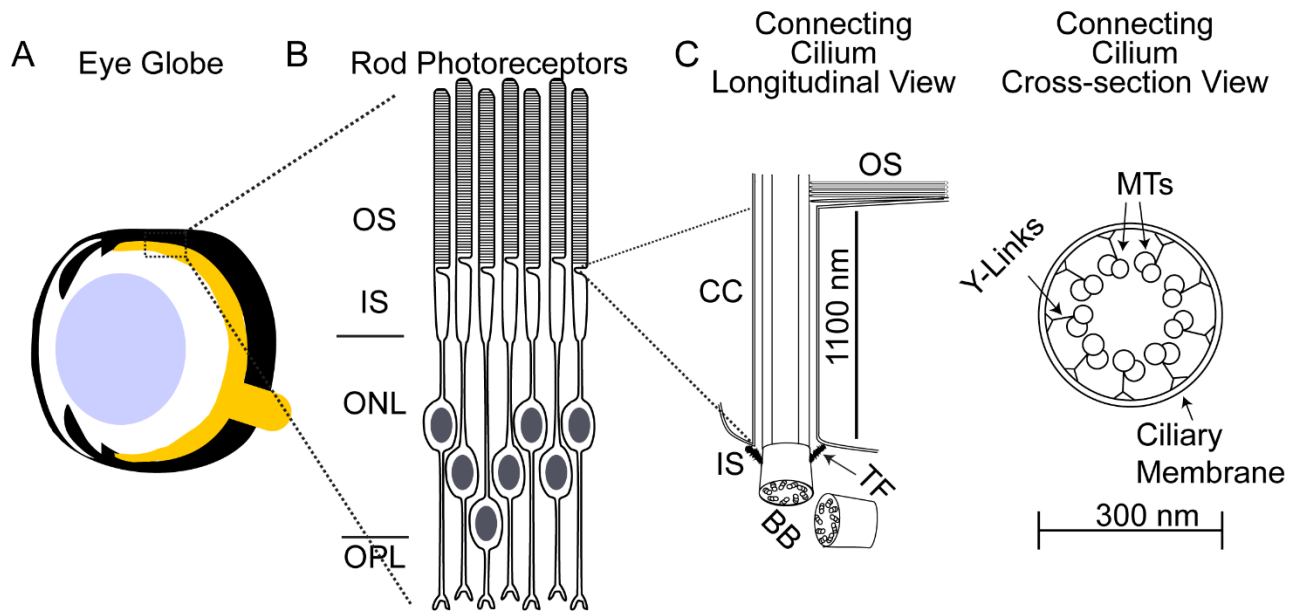


Figure 1. The photoreceptor connecting cilium. (A) The photoreceptors are the most posterior cells in the neural retina at the back of the eye. (B) Rod photoreceptor cells are distributed across four layers of the retina. (C) The connecting cilium links the outer segment to the inner segment. The dashed link shows the portion of the connecting cilium in the cross-sectional view. The dimensions of the connecting cilium are ~1100 nm by 300 nm. OS, outer segment; IS, inner segment; ONL, outer nuclear layer; OPL, outer plexiform layer; CC, connecting cilium; BB, basal body; TF, transition fibers; MT, microtubule doublets.

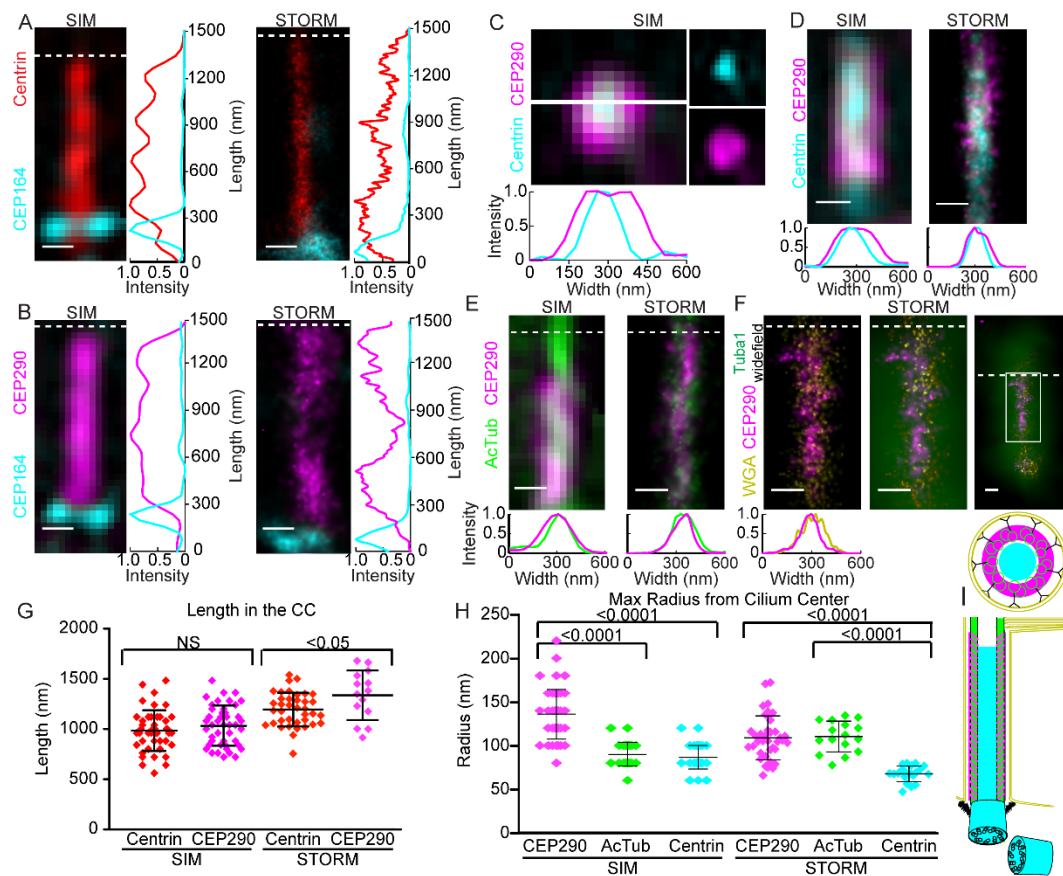


Figure 2. CEP290 localizes throughout the length of the CC and in close proximity to the microtubule doublets. (A-B) SIM and STORM images of representative cilia from adult retina, immunostained for transition fiber protein CEP164 and axonemal lumen protein, Centrin (A) or CEP164 and CEP290 (B). Row average intensity plots are shown. (C) SIM image of a representative cross section through the CC with separated channels to the right. The white line depicts the position of the average intensity line plot. (D-F) SIM and STORM longitudinal images of representative cilia immunostained for CEP290 and acetylated- α -tubulin (AcTub, E) or glycoalkaloid label WGA (F). Row-average intensity plots are shown. For CEP290/WGA labelled cilia, high and low magnification widefield Tuba1 antibody staining (green) overlay is shown. (G) Dot plot with averages and standard deviations of the lengths of CEP290 and centrin staining in the CC for SIM and STORM. (H) Dot plot with averages and standard deviations of the radii of CEP290, AcTub, and centrin in the CC for SIM and STORM. 33% of the maximum intensity value of each channel was used as the boundary criterion for the measurement of each cilium. Measurements were compared with Student's t-test and one-way ANOVA and Tukey's post-hoc test, respectively. (I) A color-coded schematic of a CC. AcTub, acetylated α -tubulin; WGA, wheat germ agglutinin; CC, connecting cilium. Scale bar 200 nm. Dotted line indicates CC/OS border. Measurements were from three different animals and SIM images of 75 cilia for CEP290, 30 for AcTub and 45 for centrin, or STORM images of 42 cilia from six animals for CEP290, 16 cilia from three animals for AcTub and 52 cilia from three animals for centrin.

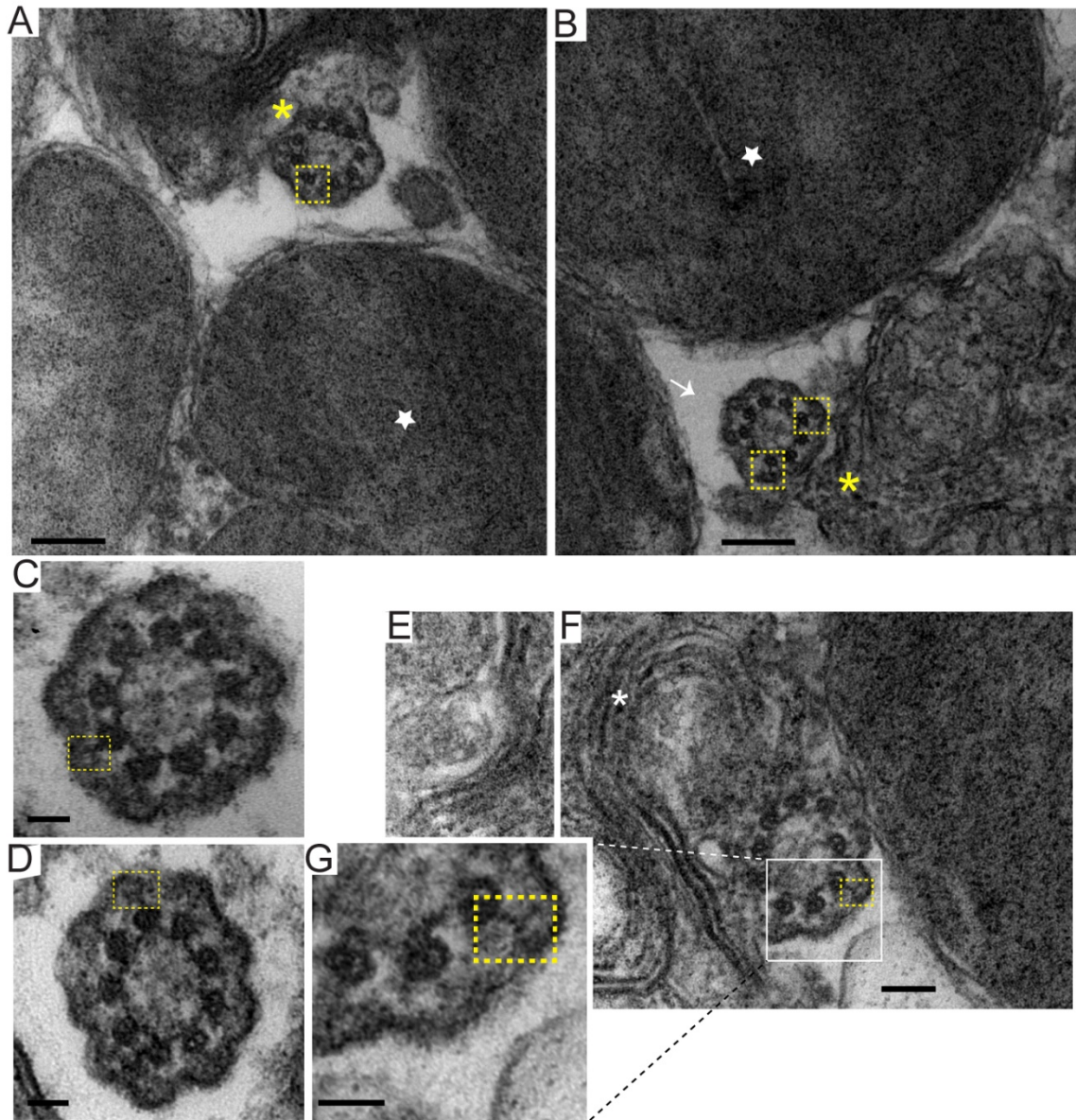


Figure 3. Y-links appear throughout the CC. (A, B) TEM image depicting the OS/ CC interface. CC (white arrow), discs *en face* (star), and cilium and discs (yellow asterisks) from photoreceptors are shown, with MT doublets connected to Y-links outlined in yellow boxes. Scale bar 200 nm. (C, D) CC from neighboring photoreceptor cells. Y-links (yellow boxes) are visible. Scale bar 50 nm. (E, F) Image of cilium and discs (white asterisk) from another photoreceptor cell. Y-links (yellow box) are visible. Scale bar 100 nm; Inset (G) scale bar 50 nm. CC, connecting cilium; OS, outer segment.

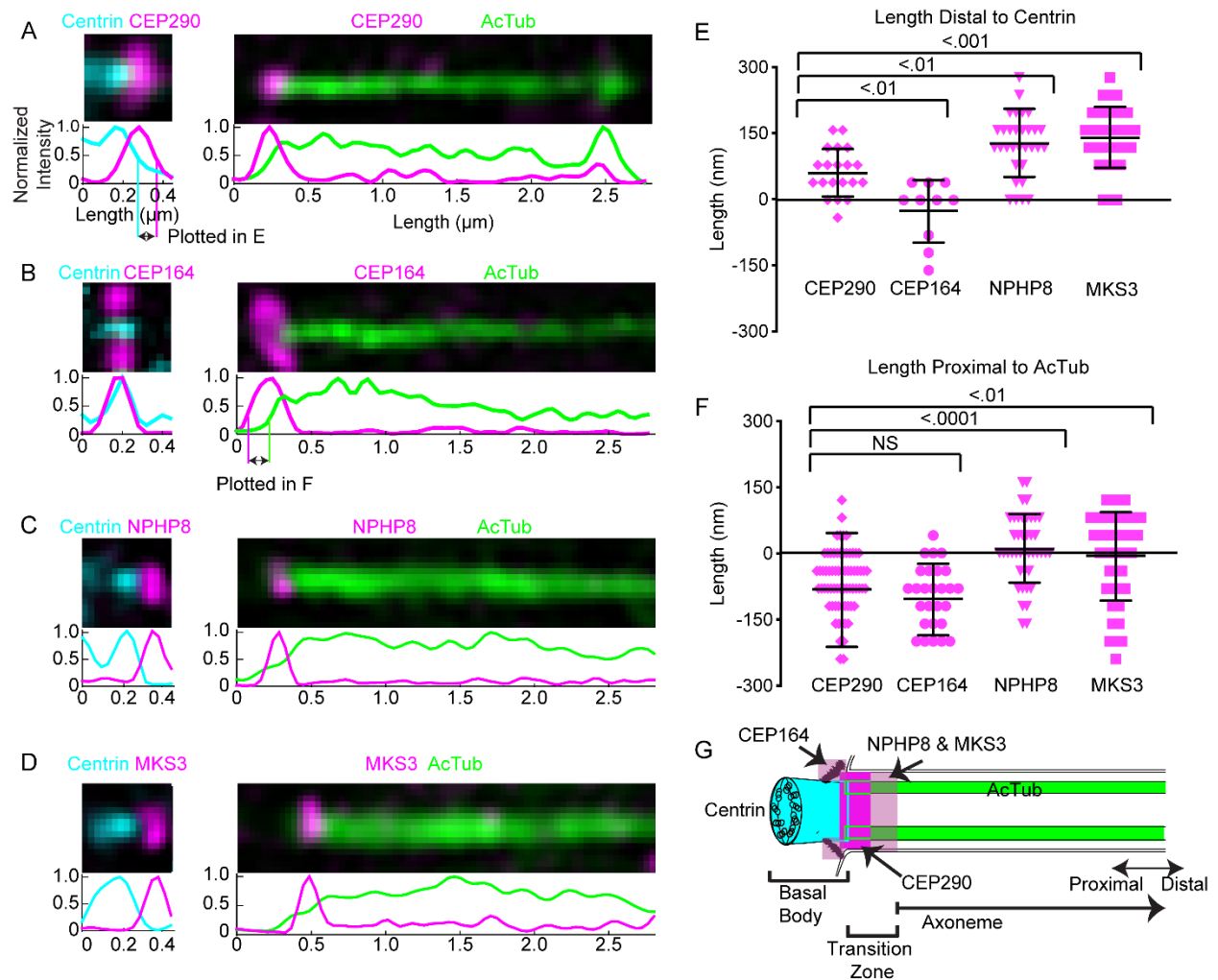


Figure 4. CEP290 localizes to the base of the primary cilium in epithelial cells. (A-D) SIM images of a representative centriole and cilium for each labeling condition, CEP290, CEP164, NPHP8, and MKS3, respectively, with centrin as a marker for the BB, and AcTub as marker for the axoneme. Row-average intensity plots are below each image. (E-F) Dot plot with average and standard deviation of the length distal to centrin (illustrated in intensity plot of A) or the length proximal to AcTub (illustrated in intensity plot of B). 33% of the maximum intensity value of each channel was used as the boundary criterion for the measurement of each cilium. Measurements were compared with one-way ANOVA and Dunnett's post-hoc test. G) A color-coded schematic of a primary cilium with results shown. AcTub, acetylated α -tubulin.

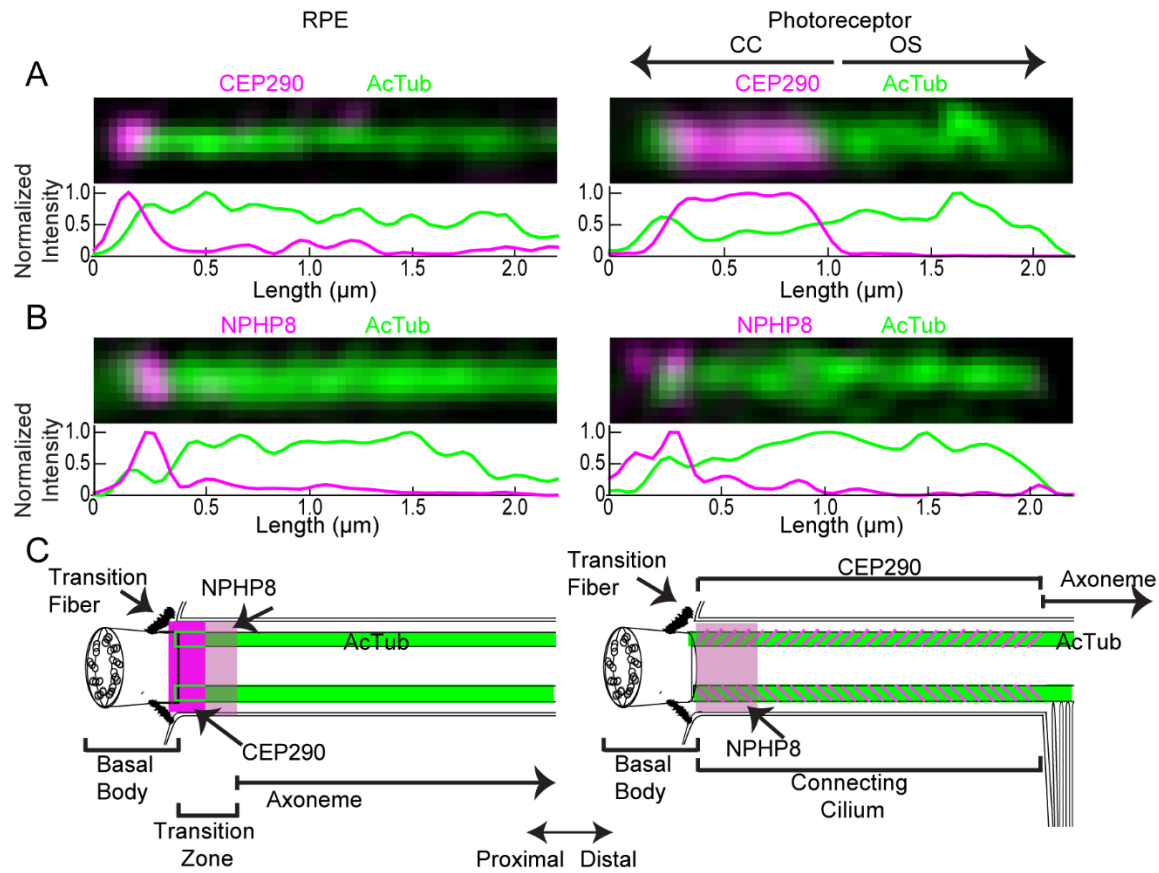


Figure 5. Comparison of ciliary protein localization in RPE and photoreceptor cilia. (A-B) SIM images depicting CEP290 and NPHP8 localization in RPE and photoreceptor cilia. Row average intensity plots are below each image. (C) A color-coded schematic of a primary cilium in RPE and photoreceptor with results shown. AcTub, acetylated α -tubulin. See also Supplemental Figure 4.

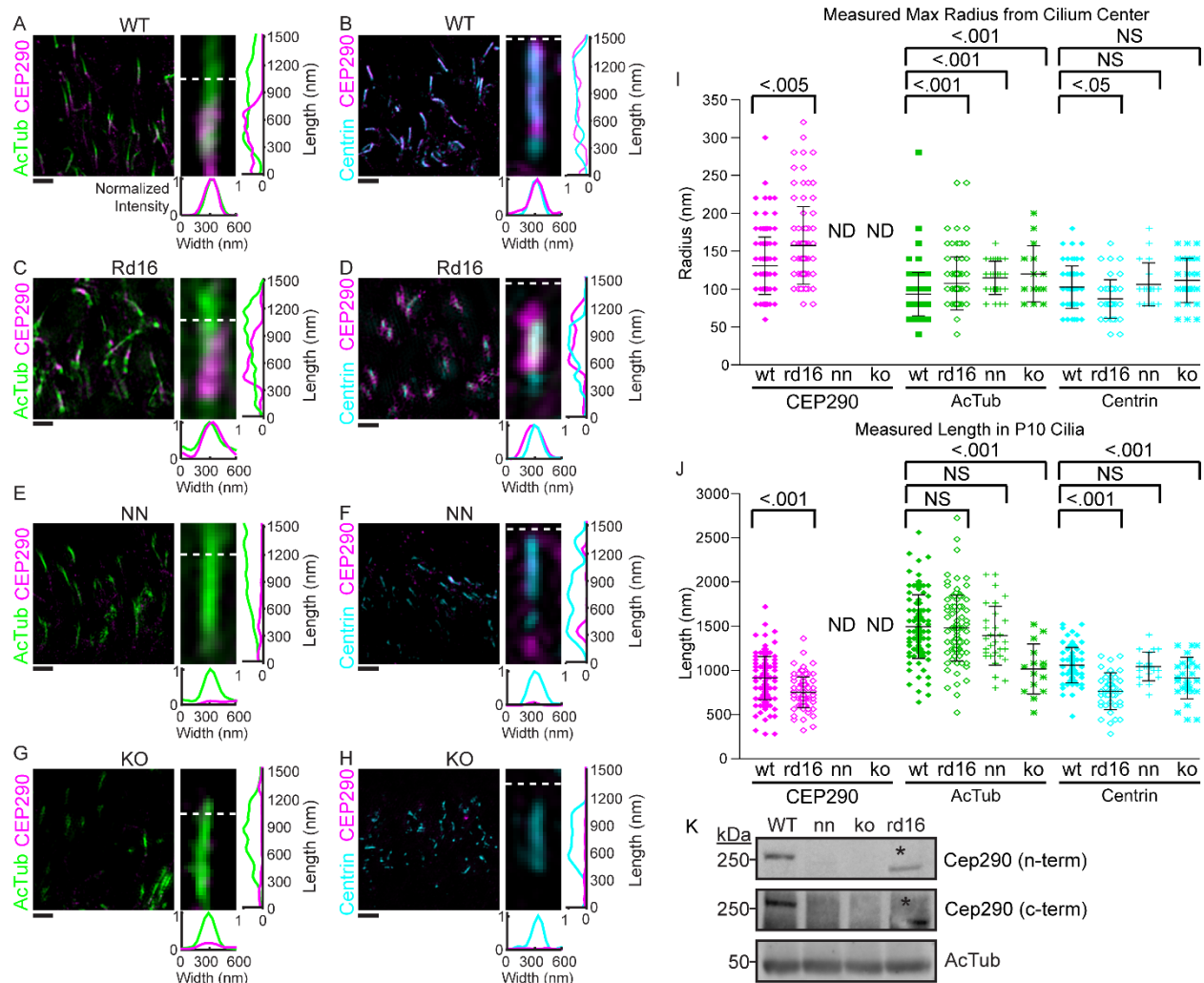


Figure 6. CC develops in *Cep290* mutant prior to degeneration. (A-H) SIM images (high magnification, right; low magnification, left) of cilia from P10 WT, rd16, NN, and KO animals labelled with CEP290, AcTub, and centrin. Scale bar on left, 1 μ m. SIM (right) images of representative cilia. Row-average intensity and column average intensity plots are shown. AcTub and centrin gains were adjusted to subsaturation for image presentation. CEP290 intensity levels in *Cep290* mutants were normalized to wild type levels (I-J) Dot plots with averages and standard deviations of the maximum radii and lengths of CEP290, AcTub, and centrin in the cilium. Cilia were imaged from three non-littermate mice for each genotype. 33% of the maximum intensity value of each channel was used as the boundary criterion for the measurement of each cilium. Measurements were compared with one-way ANOVA and Dunnett's post-hoc test. (K) Western blots demonstrating detection of CEP290 protein products. Expected sizes for WT CEP290, CEP290(rd16), and AcTub are 290kDa, 270 kDa and 50 kDa, respectively. *Asterisk indicates band shift in the rd16 protein product. Dotted line indicates CC/OS border. AcTub, acetylated α -tubulin; CC, connecting cilium; WT, wild type; rd16, *Cep290*^{rd16}; nn, near null-*Cep290*^{tm1.1Jgg}; ko, knockout-*Cep290*; ND, not detectable. The N-terminal blot lanes were run simultaneously on the same samples as the C-terminal blot

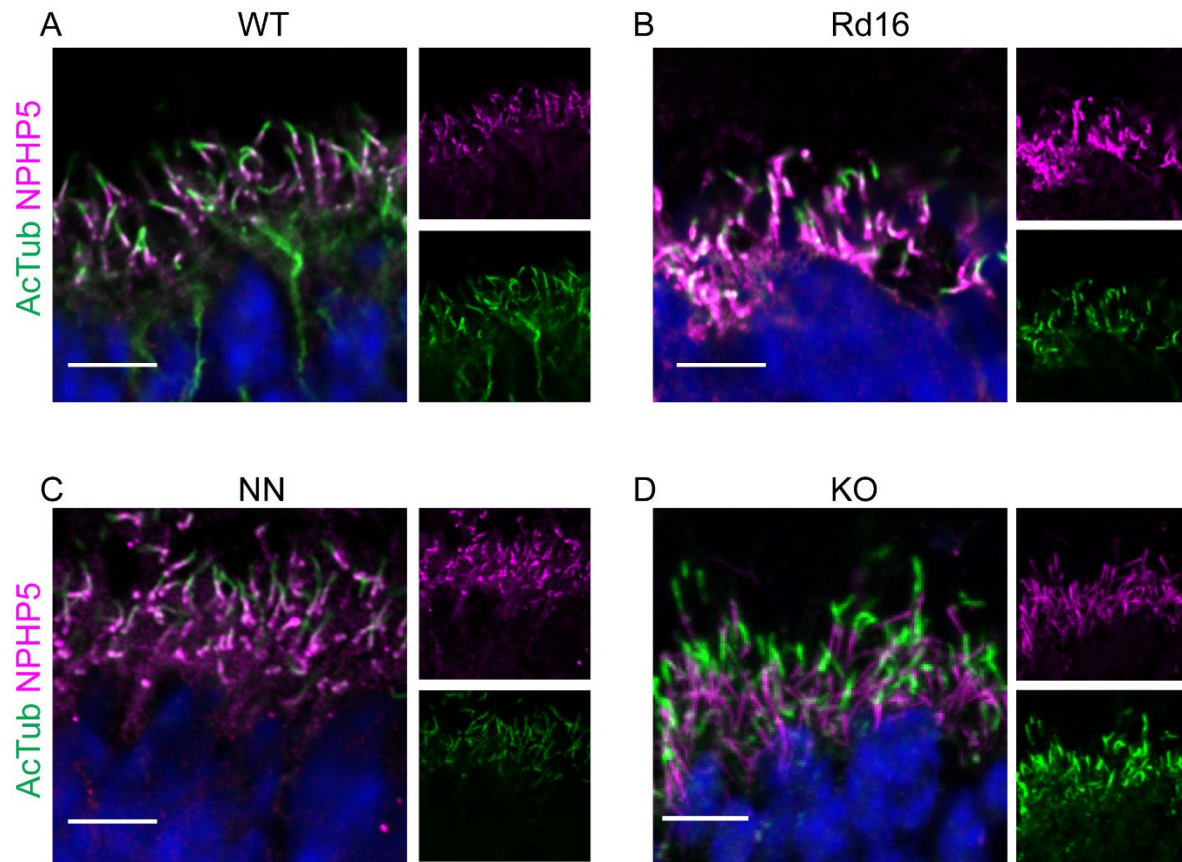


Figure 7. NPHP5 localization in WT and in *Cep290* mutants. NPHP5 antibody signal localizes to the base of the CC and the region on the rootlet and BB in WT and in *Cep290* mutant animals before photoreceptor degeneration. Confocal images of P10 WT (A), rd16 (B), NN (C), and KO (D) cilia with separated channels at low magnification to the right. WT image acquisition and processing settings were applied to WT, rd16, nn, and KO data. Scale bar 10 μ m. AcTub, acetylated α -tubulin; CC, connecting cilium; WT, wild type; rd16, *Cep290*^{rd16}; nn, near null-*Cep290*^{tn1.1Jgg}; ko, knockout-*Cep290*.

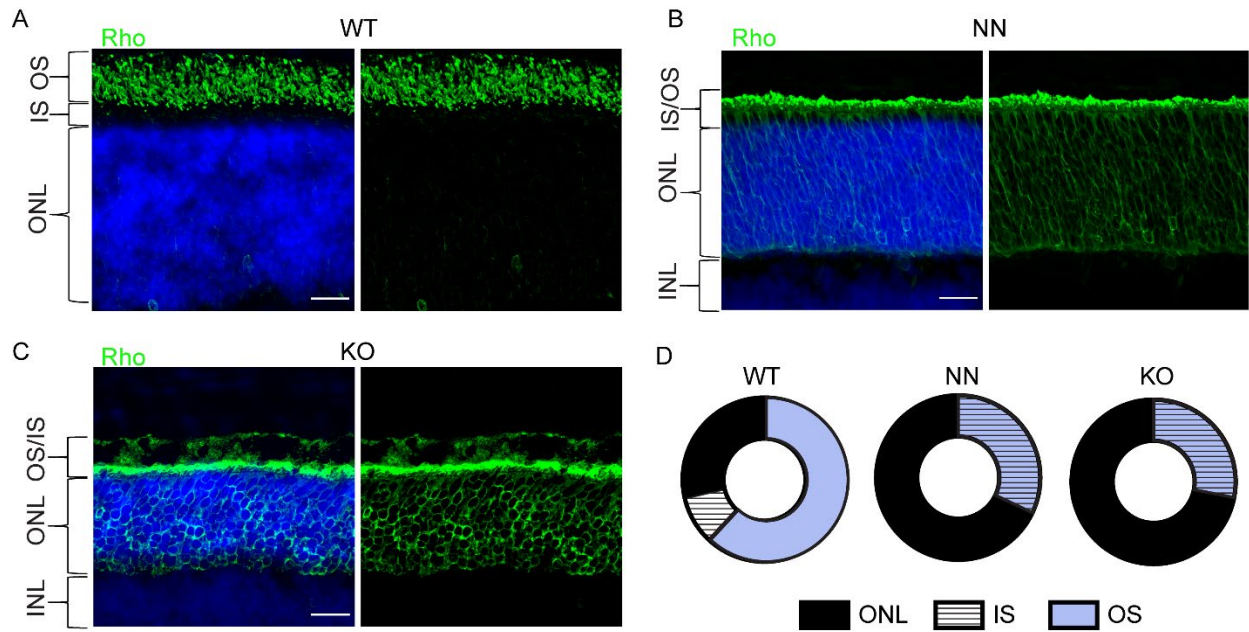


Figure 8. Rhodopsin localization in P10 *Cep290* mutant cilia. Confocal images of retina from P10 WT, NN, and KO stained for rhodopsin (green) and DAPI (nuclear stain, blue). Acquisition settings and image processing were identical for all samples. OS, outer segment; IS, inner segment; ONL, outer nuclear layer; INL, inner nuclear layer; WT, wild type; rd16, *Cep290*^{rd16}; nn, near null-*Cep290*^{tm1.1Jgg}; ko, knockout-*Cep290*. Scale bar 20 μ m. Bottom panel shows integrated intensities for each layer normalized by total rhodopsin signal for the images above.

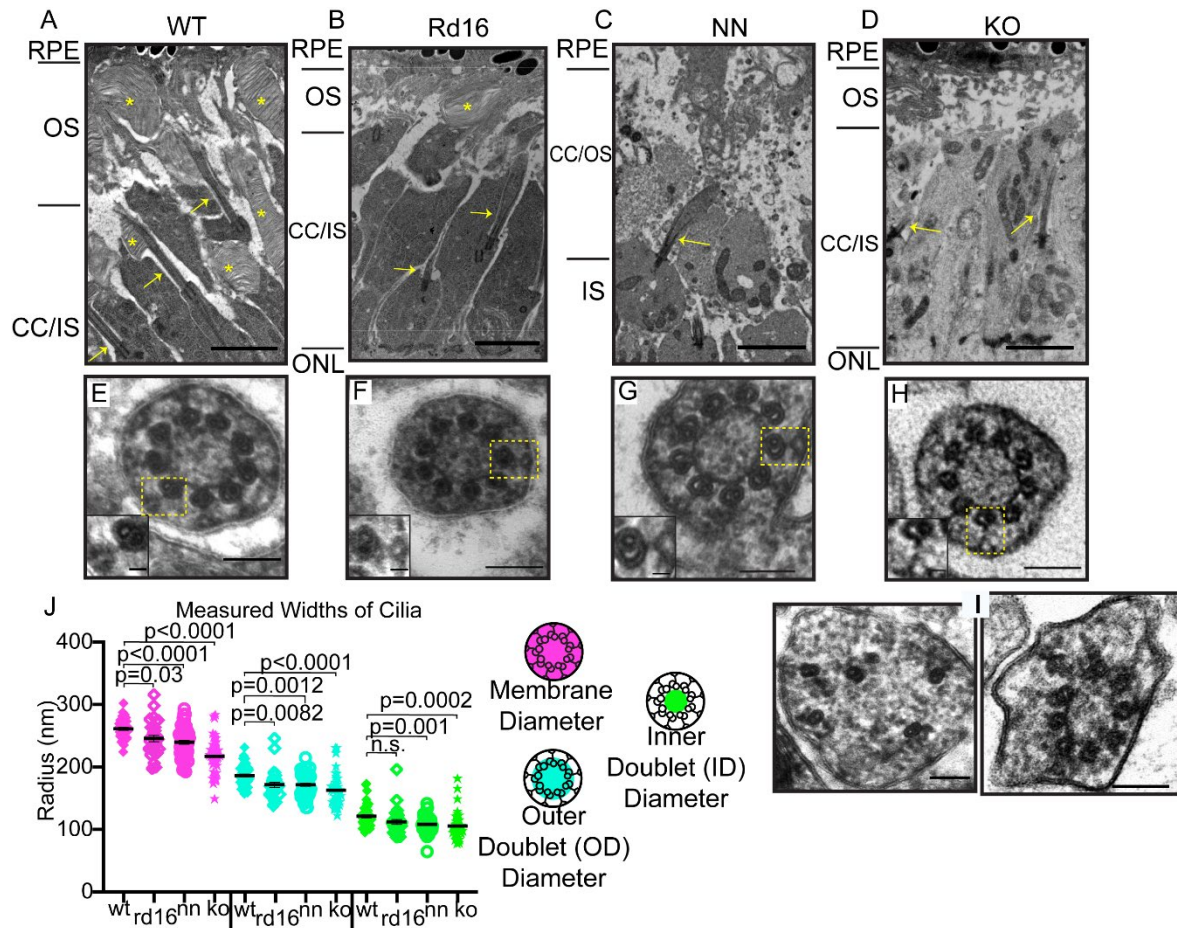


Figure 9. Y-links are present in P10 *Cep290* mutant CC. (A-C) TEM longitudinal images of P10 photoreceptor cilia from (A) WT, (B) *Rd16*, and (C) NN, and (D) KO animals depicting the (A) properly developed CC and OS, (B) rudimentary OS, and (C, D) rudimentary CC. CC (yellow arrow) and OS discs (yellow asterisk) are highlighted. Scale bar 2 μ m. (E-H) Cross section images through the CC of (E) WT, (F) *Rd16*, (G) NN, and (H) KO animals. Y-links (yellow box) are visible in WT and *Cep290* mutants. Scale bar 100 nm. Insets highlight Y-links within the box. Scale bar 20nm. Lower magnification views of the same regions of these retinas are shown in Supplemental Figure 6. (I) Cross sections through distal ends of CC showing abnormal structures in KO retinas. See also Supplemental Figure 5B. (J) Dot plot with averages and SEMs of measurements of annotated areas within connecting cilium sections from WT (43 cilia from 2 animals), *Rd16* (29 cilia from 3 animals), NN (58 cilia from two animals), and KO (44 cilia from 2 animals). Measurements were compared using one-way ANOVA with Dunnett's test.

1125

1126 **Supplemental Figure 1. Variation in the radial extent of CEP290 and WGA**

1127 **localization along the CC axis visualized by STORM.** Larger image and intensity plot

1128 are from 2F. Each highlighted region showcases 330nm in length along the original

1129 images and is accompanied by a row average intensity plot. The highlighted regions

1130 and their plots demonstrate the variability of CEP290 and WGA widths in relationship to

1131 one another throughout the cilium. Dimensions of the larger image are 1200nm x

1132 600nm, while the highlighted regions are 330nm x 600nm. Dotted line indicates CC/OS

1133 border. WGA, wheat germ agglutinin.

1134

1135 **Supplemental Figure 2. Comparisons of signals using swapped reagents.** (A) Dot

1136 plots with averages and standard deviations of radial measurements with swapped

1137 fluorophores. (B) SIM images of representative cilia from each fluorophore pairing. (C)

1138 Dot plot with averages and standard deviations of radial measurements with C- or N-

1139 terminal specific CEP290 antibodies. (D) SIM images of representative cilia labelled

1140 with antibodies identifying different CEP290 epitopes. 33% of the maximum intensity

1141 value of each channel was used to determine the boundary for the measurement of

1142 each cilium. Measurements were compared with Student's t-test with Welch correction.

1143 Dotted line indicates CC/OS border. Scale bar 200nm. AcTub, acetylated α -tubulin.

1144

1145 **Supplemental Figure 3. Time-course of CEP290 localization in rd16 mutant.** (A-H)

1146 Confocal images of retina from rd16 animals ages P7 (A), P8 (B), P9 (C), P10 (D), P11

1147 (E), P12 (F), P13 (G), and P14 (H). Low magnification image (left) shows transmitted

1148 image and AcTub and CEP290 labelled retina. Scale bar 25 μ m. Zoomed-in images
1149 (right) highlight AcTub and CEP290 labelled cilia with separate channels. Scale bar
1150 10 μ m. Retinas were imaged from littermates. Same acquisition and processing settings
1151 were applied to all data. AcTub, acetylated α -tubulin; OS, outer segment; ONL, outer
1152 nuclear layer; OPL, outer plexiform layer; rd16, *Cep290*^{rd16}.

1153

1154 **Supplemental Figure 4. Localization of NPHP8 in photoreceptor cilia.** SIM images
1155 at low (A) and high (B) magnifications showing staining for NPHP8 and acetylated α
1156 tubulin (Actub).

1157

1158 **Supplemental Figure 5. TEM images of cross-sections of CC in KO retina at P10.**

1159 (A) Upper two rows: Examples of CC with Y-links. (B) Bottom row: Examples of aberrant
1160 CC cross sections frequently seen in KO near distal end of CC. Scale bar = 100nm.

1161

1162 **Supplemental Figure 6. Low magnification Cep290 mutant transition electron**

1163 **microscopy.** Uncropped, low magnification images from P10 WT (A), rd16 (B), NN(C),
1164 and KO(D) animals; higher magnification images are presented in Figure 9. Scale bar

1165 5 μ m. Same acquisition and processing settings were applied to all data. *Asterisks - OS

1166 discs, arrow – CC, dashed lines – outer limiting membrane (IS/ONL interface). RPE,

1167 retinal pigment epithelial; OS, outer segment; IS, inner segment; ONL, outer nuclear

1168 layer; WT, wild type; rd16, *Cep290*^{rd16}; NN, near null-*Cep290*^{tm1.1Jgg}; KO, knockout-

1169 *Cep290*.

1170

1171